Final Technical Report

External Grant Award Number:
G10AP00002

Recipient:
Board of Regents of the Nevada System of Higher Education
on
Behalf of
The University of Nevada, Reno

Principal Investigators:
Ileana M. Tibuleac
Telephone: (775) 784-6256 Fax: (775) 784-4165 ileana@seismo.unr.edu
David von Seggern
Telephone: (505) 284-7672 Fax: (505) 844-7354 vonseg@seismo.unr.edu
John N. Louie
Telephone: (775) 784-4219 Fax: (775) 784-4165 louie@seismo.unr.edu

Title:
Higher resolution seismic velocity model in the Reno Basin

Award term:
12/01/2009-05/30/2011

NEHRP Element(s):
ELEMENT I: National and regional earthquake hazards assessments.
Keywords: Velocity model in the Reno-Carson basins, ambient seismic noise, Seismic zonation

Research supported by the U.S. Geological Survey (USGS), Department of the Interior, under USGS award number **G10AP00002**. The views and conclusions contained in this document are those of the authors and should not be interpreted as necessarily representing the official policies, either expressed or implied, of the U.S. Government.

ABSTRACT

There was a gap in the high resolution shear velocity models in the Reno Basin from 200 m to 3 km. Our primary goal was to fill this gap by the use of ambient seismic noise as an inexpensive alternative of active source. Tomographic studies in the Reno Basin did not allow precise control of basin depth, due to low resolution in the upper 3 km. Detailed, however very shallow velocity profiles in the Reno Basin were derived to a depth of 200 m. We estimated new constraints to improve the resolution of the velocity model in the upper 0.5-5 km from analyzing new features of ambient noise, recorded by permanent and temporary (March-July 2008) instrument deployments. An accurate shallow velocity model in the Reno Basin was important for understanding of earthquake ground motions and their variability in the Reno and Carson City region and for realistic quantification of seismic hazard. Geologic evidence in this region indicated the potential for large magnitude (M7-7.5) events occurring on local faults, such as the Mt. Rose and Genoa Faults.

We used for our studies the permanent Reno-Carson City seismic network, a temporary Rapid Array Mobilization Program (RAMP) deployment and a deployment of high frequency geophones with "Texan" digitizers. The temporary stations were deployed in 2008 by the Nevada Seismological Laboratory in the Reno Basin to record a very shallow (< 4 km deep) earthquake sequence occurred in west Reno. We calculated ambient noise and signal autocorrelation and crosscorrelation to recover the surface waves and P reflections from ambient noise-derived Green's functions between pairs of these instruments. The estimated shallow seismic velocity model was integrated with the existing Reno Basin velocity model, providing information within three km from the surface.

Our report has two parts, as follows:

Part 1. *Development of methods for computing Green's Functions from ambient noise recorded by accelerometers, analog, broad and narrow-band seismometers, seismometers;*

Part 2. *A higher resolution seismic velocity model in the Reno Basin estimated from ambient - seismic noise.*

<u>Author contributions</u>: Dr. Tibuleac analyzed the waveforms, derived the velocity models and wrote the final report, and the two publications describing the research. Dr von Seggern has written and supported the ambient noise processing codes, has contributed to the research publications and reviewed the final report. Two students, Nick Steele and Griffin Burke-Ruhl were trained on the project and helped with data analysis. Dr John Louie has consulted in relation with the Reno-Carson Community Velocity Model.

Part 1.

Development of Methods for Computing Green's Functions from Ambient Noise Recorded by Accelerometers, Analog, Broad and Narrow-Band Seismometers, Seismometers

I. M. Tibuleac, D. H. von Seggern, J. G. Anderson and J.N. Louie,
Nevada Seismological Laboratory, U. Nevada, Reno NV 89557
ileana@seismo.unr.edu;vonseg@seismo.unr.edu;jga@seismo.unr.edu;louie@seismo.unr.edu;

INTRODUCTION

The objective of our study is to supplement the regional P/S 3-D velocity model in the Reno Basin with shear-wave velocity models derived from ambient noise interferometry (Aki, 1957; Claerbout, 1968; Shapiro et al., 2005; Sabra et al., 2005; Lin et al., 2008; Yang et al., 2008). We use a variety of seismic sensors in the Reno-Carson area (Figure 1).

There is a gap for demonstrated extraction of Green's Functions (GF's) from ambient noise between short and long inter-station distances. The lateral resolution of existing tomographic models exceeds the dimensions of the Reno Basinarea (~ 60 km^2), and their depth resolution is larger than the Reno Basindepth to basement (< 3 km). GF's have been recently retrieved in the western USA from data recorded at broadband sensors, such as the EarthScope Transportable Array deployment (Figure 1, lower right plot) with lateral resolution of 60-100 km (Yang et al., 2008; Lin et al., 2008) and for periods exceeding 8 s (i.e. sampling more than 8 km deep). Using the Re-Mi methods, noise-extracted Rayleigh waves for local shallow shear-wave velocity studies provided information on structure less than 0.2 km from the surface (Scott et al., 2004). In order to estimate P and S velocity models deeper than 3 km, earthquake tomography was until recently the only cost effective alternative to active source experiments (Frary et al., 2009). The body-wave tomographic studies in the REno Basin (Preston and von Seggern, 2008) do not allow precise control of the velocity or depth of shallow structures in the basin, due to low resolution in the upper 3 km. Another disadvantage of body-wave tomography is the high level of uncertainty in the S-arrival time picks. GF extraction from noise cross-correlations at scales less than 60 km using non-broadband instruments is possible and has been recently demonstrated by several research groups (Picozzi et al., 2009; Gouedard et al., 2008; Cho et al., 2007).

To obtain higher resolution three-dimensional models at less than 60-km scale, using ambient noise-extracted GF's, the density of broadband (here named BH, from the three-component SEED channel names) stations must be increased considerably. Such deployments of broad-band instruments are not cost-effective. Alternatively, all the instruments available in the region must be used. The advantage of Reno Basin as a populated region is that, in addition to broadband sensors, dense networks of short-period instruments (analog or digital) and of accelerometers are already deployed (Figure 1, left

plot). This allows analysis of hundreds more inter-station paths, with the potential to greatly improve velocity-model resolution.

We define as "unconventional" a sensor pair containing at least one non-broadband sensor or at least an analog short-period sensor. As shown below, extracting useful data with ambient noise interferometry from unconventional sensor pairs is not a trivial exercise. Few research groups have attempted this type of study, and to our knowledge, only one group used accelerometers (Cho et al., 2007).

The first challenge in using unconventional sensor pairs is data quality. Short-period recordings often have poor data quality for the desired frequencies, especially "analog" recordings. The short-period instruments are predominantly narrow-band (corner frequency ≥1 Hz) with the response rapidly decreasing at periods longer than 1 s. The accelerometer response de-emphasizes low frequencies (< 1 Hz) because it falls off as the inverse of period squared. Also, accelerometers usually operate in trigger mode. In this study we show recovery of GF's from ambient noise for sensor pairs including: 1) digital narrow-band seismometer (EH) recordings (for instance, S-13 seismometer), 2) analog narrow-band seismometer (SH) recordings, digitized after transmission, 3) digital accelerometer (HG) recordings and 4) digital broadband instrument (BH) recordings, including USArray stations. Each of these instrument classes presents its own problems for GF recovery and requires appropriate processing.

The second significant challenge in using high-density unconventional sensor pairs is that measurements of Rayleigh-wave phase and group velocity are difficult for stations separated by less than 15 km. The "rule of thumb" is that the longest Rayleigh wavelength that can be well-resolved is one-half to a one-third of the inter-station distance. For example, at 15 km distance, in order to extract 3 km/s group velocity Rayleigh waves from ambient-noise cross-correlations, noise spectra should contain sufficient energy at periods shorter than ~2 s.

The third challenge may be the ambient noise frequency content in Reno Basin, which lies at distances of at least 300 km from the coast. In this area, if all the ambient noise were of oceanic origin, retrieving Rayleigh waves at periods shorter than the microseismic range (6-12 s) would be very difficult, because the energy at these periods is low. Fortunately, although oceanic noise is the main ambient noise source, not all the ambient noise has oceanic origin (Frank et al., 2009). The advantage of populated regions is the presence of shorter-period cultural noise. Groos and Ritter (2009), observed that human activity is a dominant influence on the broad-band urban seismic noise in the Bucharest, Romania area, in all frequency ranges from 0.04 Hz to 45 Hz. These authors did show that the urban noise may have localized maxima, which affect GF extraction. If such a maximum is on a line perpendicular to the inter-station distance, GF extraction will likely be affected more than if the maximum is approximately on the same line with the two stations. Also, the advantage of rapid topographic changes, such as with the Sierra Nevada in the Reno Basin vicinity, is an increase in short-period noise due to wind and due to topography scattering. The Reno-Carson City network is installed in an area of high natural seismicity, thus with higher levels of earthquake coda-related seismic noise.

When used in ambient noise studies, the Reno Basin deployment has several other advantages: 1) it includes densely spaced stations, thus the depth range that can be resolved by Rayleigh waves is shallower (1 - 7 km); 2) data is readily available (continuous recordings are available for accelerometers in Reno) and 3) data problems, if any, are well-known.

Our method includes: 1) Application of crosscorrelation algorithms (based on the work by Bensen et al., 2007) to extract GF's. Our new data processing approach includes transformation of all waveforms into broadband velocity records, spectral whitening and continuous waveform pre-filtering as a function of inter-station distance and instrument type. 2) GF's analysis using frequency-wavenumber (FK) plots obtained by delay-and-sum methods at arrays of close stations. These techniques are applied on GF's extracted between a virtual source, i.e. a station (at 15 - 160 km distance) and adhoc arrays (aperture less than 15 km) within the RReno Basin. Ad-hoc arrays include the ANSS accelerometers in Carson City (Table 4), the ANSS array in Reno (Figure 1, left plot) and the Mogul RAMP broadband array (Figure 1, right plot). 3) Phase velocity dispersion curve inversion for first-order shear velocity models using the Computer Programs in Seismology surf96 (Herrmann and Ammon, 2002).

DATA

We process continuous waveforms recorded from 2007 to 2009 at Nevada Seismological Laboratory (NSL) and at EarthScope TA stations in Nevada. Waveforms are recorded at a sample rate of 20 sps or higher. The permanent instrumentation deployed in the Reno Basinand vicinity consists of 1) an Advanced National Seismic System (ANSS) array of 21 stations, continuously recording, with accelerometer (HG) sensors in Reno and Carson City; 2) several NSL digital short-period (EH) sensors; 3) several analog–transmission short-period sensors (SH) and 4) three broadband (BH) sensors (Figure 1, left plot). This setting (~ 60 km in scale) is smaller than the broadband networks of hundreds of km aperture usually used for GF retrieval (Figure 1, lower right plot). The Reno Basin network includes (Figure 1, upper-right plot) a temporary Rapid Array Mobilization Program (RAMP) array of portable broadband stations, named the Mogul Array. This ~ 4 km aperture array was installed in Mogul, west of Reno, to record an earthquake swarm in 2008 (Anderson et al., 2009).
To illustrate data quality, we also use continuous waveforms recorded at stations within the Southern Great Basin Digital Seismic Network (SGBDSN) in 2007 and 2008 because they have the advantage of co-located HG, SH and EH sensor deployments.

METHOD

We base our method on the fundamental observation that if A and B are two passive sensors (seismic stations), the GF, or the signal which B would receive when A is given an impulsive excitation, can be recovered from the temporal cross-correlation of incoherent noise received in A and B (Wapenaar, 2004; Sanchez-Sesma and Campillo, 2006). Because this signal is usually deeply buried in the ambient noise at random times

and with random amplitudes, summation of the cross-correlations over a long time (months to years) is necessary to retrieve the GFs.

Green's Function retrieval from "unconventional" sensor pairs

The unconventional deployments have significant disadvantages for GF extraction:
1. Narrow-band analog recordings (SH) typically have a very narrow usable pass-band, with less accurate measurement of true ground motion at low frequencies (f < 0.2 Hz) and have records often plagued by spikes and dropouts. The combination of seismometer response roll-off at f < 1 Hz and of too few counts per volt of seismometer output can lead to inadequate measurement of true ground motion. The records are also affected by data-logger noise and transmission noise.
2. Short-period digital recordings (EH) are predominantly narrow-band (corner frequency >= 1 Hz) with response rapidly decreasing at frequencies lower than 1 Hz. Again, too few counts per volt of seismometer output will inadequately measure the true ground motion at frequencies below the corner.
3. Investigations using accelerometer recordings (HG) must overcome several obstacles. The existence of spurious noise, or "bad noise", plagues many accelerometer recordings. A very large diurnal drift due to ambient temperature changes exists. The instrument response discriminates against faithful recording of low-frequency ground motion, and removal of the instrument response to obtain velocity or displacement is not a trivial correction. The displacement derived from accelerometers is often unstable at long periods, as a double integration is required. Accelerations at long periods are very small, less than the instrument noise, thus the signal-to -noise ratio is low. Unlike the Reno Basin ANSS deployment, accelerometers in other locations usually operate in trigger mode.
Thus, the response of all three types of sensors is reshaped to a broad-band sensor response with a corner at 10-s period, after being high-pass filtered at 0.05 Hz.

Tests for Method Development

The first test was aimed at identification of "good" versus "bad" noise. “Good” noise is usually Earth seismic noise, cultural noise and atmospherically induced noise. In order to obtain the same results with different types of sensors, the recorded noise should be coherent, within the frequency range of interest, at the same location. Our investigations show that accelerometer-recorded noise at periods longer than 1 s is not well correlated with the noise recorded by short-period instruments in the same frequency band.
A comparison of waveforms recorded at three different types of sensors is shown in Figure 2A. These co-located sensors are currently operating at the SGBDSN station Wildcat (WCT/WLD) in southern Nevada, near Yucca Mountain. In Figure 2A only the EHZ and SHZ traces show coherent long-period energy from 0.1 to 1 Hz. Figure 2B shows that the HG sensor noise spectrum from 0.1 to 1 Hz, is different from the observed noise spectrum of the EH and SH. A good measure of whether recordings from differing instruments are reproducing ground motion is coherence. We use the Matlab$^{@}$ function "mscohere" for the magnitude squared coherence estimate of two signals, using Welch's averaged, modified periodogram method (Stoica and Moses, 1997). The magnitude

squared coherence (called "coherence" here) estimate is a function of frequency with values between 0 and 1 and indicates how well the two signals correspond to each other at each frequency. Figure 2C shows that the EHZ and SHZ components are recording ground motion above instrument noise levels for frequencies below 1 Hz. At these frequencies, the lack of coherence of the EHZ-HGZ and SHZ-HGZ components shows that the HGZ component recordings are affected by internally generated/self-noise (sensor and/or digitizer noise). The presence of HG instrument noise is indicated by 1) low coherence with the two velocity sensor components, 2) constant noise spectrum variance observed after the instrument is removed, and 3) by the shape of the HG spectrum, resembling the shape of a white spectrum convolved with the response of a broadband seismometer.
Instrumental noise can make the recovery of GF's from continuous HG data difficult. When earthquake seismic signal is present, it is well-known, however, that longer-periods (> 5 sec) are recorded by accelerometers. This observation is important because most accelerometers are operating in trigger mode. As shown by Yao et al. (2006,2008), using only event records on broadband stations can lead to extraction of GF's similar to those extracted from continuous noise. Thus, because records with Earth signals are useful, accelerometers could be successfully used for GF's retrieval, even in trigger mode, provided that enough triggered data is available.

To assess improvement in the GF signal-to-noise ratio (SNR) with an increase of the time length, we performed a second test for a pair of SH sensors, SMI and TAH (Figure 3 and Table 4). Like with broadband sensors (Bensen et al., 2007), good results are produced after stacking three months of data. For best GF SNR, however, stacking of cross-correlations from analog sensors needs to be for longer than three months, preferably one year or more. In this study, we stack crosscorrelations over a two-year period, to ensure the best GF SNR.
The approach we take in processing unconventional sensor-pair records includes:
1) Appling high-pass signal filtering at 0.05 Hz with a zero-phase, 4-pole Butterworth filter to remove accelerometer record drift;
2) For all sensors, reshaping the response to a broad-band velocity sensor response with a corner at 20-s period. We have chosen the 20-s period since 20-s fundamental mode Rayleigh waves are the longest-period waveforms we expect at inter-station distance less than 100 km. This procedure also addresses the signal distortion resulting from accelerometer instrument removal (Iwan et al., 1985);
3) Choosing additional, specific pre-filtering frequency bands as a function of inter-station distance;
4) Using longer windows (one year or two) of continuous data for short-period instruments;
5) Using the Bensen et al. (2007) sign-bit convention, with pre-whitening (all positive amplitudes = +1 and all negative amplitudes = -1);
6) Folding the negative time lags of the stacked crosscorrelations over to the positive time lags and display and analyze the mean as the extracted GF's.

<u>Green's Function processing</u>

To avoid spatial aliasing, the “rule of thumb” is that the shortest wavelength is half the minimum receiver spacing. Thus, the longest Rayleigh wavelength was chosen between half and one third the largest receiver distance. The depth probed is usually 1/3 of the Rayleigh wavelength. For inter-station distance less than 15 km, for the ANSS stations, we form adhoc arrays of stations, and we estimate the fundamental-mode Rayleigh phase velocity from uniformly sampled points in frequency-wavenumber space (FK). At each frequency, the waveforms are narrow-band filtered using a "Meyer" wavelet (Tibuleac and Britton, 2006; Tibuleac and Herrin, 1999) and Continuous Wavelet Transforms (CWT); then they are beamed for a range of discrete, regularly-spaced wavenumbers. The maximum energy in the beam becomes the amplitude for a given F-K point. Time-domain crosscorrelation (Tibuleac and Herrin, 1997) is used to estimate fundamental mode Rayleigh phase velocity across the Mogul array. The phase velocity curves are inverted with the Computer Programs in Seismology (CPS3.3) (Herrmann and Ammon, 2002).

RESULTS

GF retrieval for narrow-band analog recordings (SH) paired with SH, BH, and HG sensors.

In Figure 4 we show that GF’s can be recovered from narrow-band analog records at least in the microseismic frequency band. Station locations and path information are listed in Table 4. Although analog stations have only vertical components, there is a significant amount of new information that can be extracted from the estimated GF’s. To avoid spatial aliasing, the shortest wavelength that can be analyzed is approximately half the minimum receiver spacing. The longest wavelength was chosen between half and one third the largest receiver distance.

GF retrieval for broadband recordings (BH) paired with SH, BH, and HG sensors.

In Figure 5 we show GF’s retrieved for paths from the broadband sensor P07A to stations in the Reno area (Figure 5A) and from PAH (Figure 5B) to ANSS accelerometers in the Carson City area, south of Reno. When compared to the Priestley and Brune (1978) model, both transects show lower phase velocity. Lin et al. (2008) also observe slightly lower Rayleigh phase velocity at periods larger than 8 s (i.e. sampling deeper than 8 km), when compared to the average measurements at each period, in the Reno-Carson area.

We find very good correspondence of the longer period (5 - 10 sec) of the GF's extracted on similar paths from a BH-HG and a BH-BH pair (Figure 6). The paths are from the TA station P06A to BMHS (BH) and to the accelerometer PICO (HG) (see also the line in Figure 1). BMHS and PICO are within 1 km of each other.

GF retrieval for pairs of closely-spaced sensors (array aperture < 15 km).

To obtain information beneath adhoc arrays of stations within the REno Basin, we consider stations outside the Reno Basin area as virtual sources, with the empirical

requirement that the array aperture is less than one fifth the virtual source-array distance. We use the array processing methods described earlier to analyze GF's recorded at the array stations from the virtual source. We estimate the fundamental-mode Rayleigh phase velocity across the adhoc arrays. As shown in Figures 4-8, the GF Rayleigh waves are relatively narrow-band, with period depending on the path length. The longer the inter-station distance, the longer is the period resolved (which still satisfies the far-field approximation); thus GF's retrieved on longer paths allow deeper sampling of the structure beneath the array. For each station considered as a virtual source, the extracted GF record section is shown in the left plot and phase velocity dispersion curve information for the corresponding adhoc array is shown in the right plot. The FK results for the ANSS stations are shown in Figure 7, and Figure 8 shows the time-domain crosscorrelation results for the Mogul array.

Retrieval of the GF P-phase.

Although *P*-arrival retrieval is not the scope of our study, and thus we took no data-processing alternatives aimed at P-arrival extraction, we interpret as GF *P*-arrivals the phase observations in Figures 3B, 8B, 8D and 9B. In figures 3B and 9B we identify P-arrivals using the *P* group velocity. The *P*-arrivals in Figure 8 (B and D) are identified using horizontal velocity and back azimuth estimated from crosscorrelation in time domain (Table 1). *P* - arrivals are observed at a variety of sensors (Figure 3B, 9B, 8B and 8D). If these *P*-arrivals would be "ghosts" from scatterers lateral to or beneath an inter-station path, 1) they would be path-characteristic; 2) they would not occur for multiple paths; 3) they would not line up at Pn/Pg arrival time; 4) even if they would occur for multiple paths, they would not have Pn/Pg velocity and back azimuth when analyzed at a 4 km aperture array. Since Rayleigh waves are also observed at the *P*-arrival frequencies, we do not believe this is an artifact of the sensor response. The P-arrival horizontal velocity extracted in Table 1 has been used as a constraint in the inversion for shear velocity models.

First-order shear velocity models in the Reno Basin and in the Reno-Carson City area.

Using the CPS3.3 algorithms , we invert the interpolated phase-velocity measurements to derive shear-velocity models beneath the 4-km aperture Mogul array (Figure 8C), beneath the 10-km aperture ANSS array (Figure 10A) in the Reno Basin and beneath the 15 km aperture ANSS array in the Carson City basin (Figure 10B, Table 4). A summary of the fundamental mode Rayleigh phase velocity curves for the Reno - Carson area is shown in Figure 10C. The starting model (Table 3) is similar to the model derived by Priestley and Brune (1978).

As shown in Figures 8B and 10, the phase velocity beneath each array varies within roughly 0.5 km/s of the estimated value at each period. Possible explanations of these variations are variability of GF's sampling paths (wavelengths at these periods are comparable to the relief variations in Nevada), period-dependent noise source anisotropy (Tsai, 2009), and/or the structural variability across the array at different back azimuths.

Shear velocity models in the Reno-Carson City area (Table 3) are derived using the interpolated values of the phase velocity. Measurements are available for periods between 1.5 s and 10 s. The estimated first-order shear-velocity models (global and beneath each array) are shown in Table 3. The shear velocity value derived for the upper 1-km thick layer of the Reno Basin is 1.4 km/s. According to results of a study by Campbell (2009), this value is consistent with shear velocity in sedimentary basins at more than 600-m depth and is lower than the hard-rock shear-wave velocity of approximately 2 km/s.

CONCLUSIONS

We recover GF's from cross-correlation of ambient noise data in the Reno-Carson city area using continuous data recorded at unconventional sensors, as opposed to using only the three broadband seismometers available in the area. We process analog narrow-band seismometers, digital narrow-band seismometers, and accelerometers from the NSL seismic archive. Each sensor type needs a specific processing approach. In all cases, we reshape the sensor responses to that of a broadband seismometer.

We show that we can obtain useful fundamental mode Rayleigh phase velocity dispersion data in the period range of 1.5-10 s from pairs of unconventional sensors, or from a broadband sensor paired with an unconventional sensor, by processing ambient-noise cross-correlations. Our results show that enough noise energy is recorded at periods shorter than 10 s to extract GF's. We observe 0.5 km/s phase velocity measurement variability at the same location and at the same period. The errors are possibly due to path heterogeneity and/or to period-dependent noise source anisotropy. We have encouraging results in identification the P phase of the GF's, although the observed P-phases have low SNR.

Using array processing, we obtain an average velocity model beneath ad-hoc arrays of instruments within 15 km of each other. Our procedure is suitable when the frequency content of the waveforms does not allow direct analysis of the inter-station GF's and provides information on deeper layers beneath the ad-hoc array (of the order of km), as opposed to information in the upper 200 m.

The estimated dispersion results show fair agreement with dispersion curves previously published for the Great Basin; however, as expected, the phase velocity is lower at a range of shorter periods. Within the Reno Basin and the Reno-Carson City area, we estimate shear-velocity values which are consistent with known basin geological structure.

REFERENCES

Aki K., 1957. “Space and time spectra of stationary stochastic waves, with special reference tomicrotremors”, Bull. Earthquake Res. Inst. Tokyo Univ. : 35, 415-456.

Anderson, J. G., I. Tibuleac, R. Anooshehpoor, G. Biasi, D. von Seggern and K. Smith 2009. Exceptional Ground Motions Recorded During the 26 April, 2008,

MW=5.0 Earthquake in Mogul, Nevada, Bull. Seism. Soc. Am., 99, No. 6, 3475–3486, doi: 10.1785/0120080352

Bensen, G.D., M.H. Ritzwoller, M.P. Barmin, A.L. Levshin, F. Lin, M.P. Moschetti, N.M. Shapiro, and Y. Yang., 2007. Processing seismic ambient noise data to obtain reliable broad-band surface wave dispersion measurements, Geophys. J. Int. 169, 1239-1260.

Claerbout J. F., 1968. Synthesis of a layered medium from its acoustic transmission response, Geophysics, 33, 264-269.

Cho, K. H., R. B. Herrmann, C. J. Ammon, and K. Lee, 2007. Imaging the Upper Crust of the Korean Peninsula by Surface-Wave Tomography, *Bull. Seism. Soc. Am.*, **97**, No. 1B, 198–207, doi: 10.1785/0120060096.

Frary, R.N., Stephenson, W.J., Louie, J.N., Odum, J.K., Maharrey, J.Z., Messmer, M.L., Tomlinson, I., Littlefield, E.F., Hughes, A., Jha, S., Kohls, K., Dhar, M.S., Konkol, S., Wakwak, A., Cashman, P.H., Trexler, J.H., Kent, R., Hoffpauir, C., 2009. Preliminary analysis of high-resolution seismic imaging profiles acquired through Reno, Nevada, for earthquake hazard assessment, Abstract.

Frank, S. D., A. E. Foster, A. N. Ferris, and M. Johnson, 2009. Frequency-Dependent Asymmetry of Seismic Cross-Correlation Functions Associated with Noise Directionality, *Bull. Seism. Soc. Am.*, **99**: 462-470

Herrmann, R.B., Ammon, C.J., 2002. Computer Programs in Seismology – SurfaceWaves, Receiver Functions and Crustal Structure. Saint Louis University, http://www.eas.slu.edu/People/RBHerrmann/ComputerPrograms.html.

Guedard P., L. Stehly1, F. Brenguier, M. Campillo, Y. Colin de Verdiere, E. Larose1, L. Margerin, P. Roux, F. J. Sanchez-Sesma, N. M. Shapiro and R. L. Weaver, 2008. Cross-correlation of random fields: mathematical approach and applications, *Geophysical Prospecting*, 2008, **56**, 375–393.

Groos, J. C. and J.R.R. Ritter, 2009. Time domain classification and quantification of seismic noise in an urban environment, Geophys. J. Int., doi: 10.1111/j.1365-246X.2009.04343.x

Iwan, W. D., M. A. Moser, and C.-Y. Peng, 1985. Some observations on strong-motion earthquake measurement using a digital accelerograph, Bull. Seismol. Soc. Am. 75, 1225–1246.

Lin, F. C., Moschetti, M. P. & Ritzwoller, M. H., 2008. Surface wave tomography of the western United States from ambient seismic noise: Rayleigh and Love wave phase velocity maps. *Geophysical Journal International* 173, 281-298.

Preston, L., and D. von Seggern, 2008. Joint Seismic Tomography/Location Inversion in the Reno/Carson City Area, Final Report to the National Earthquake Hazard Reduction Program, U. S. Geological Survey Award Number 07HQGR0022.

Picozzi, M., S. Parolai, D. Bindi and A. Strollo, 2009. Characterization of shallow geology by high-frequency seismic noise tomography, Geophys. J. Int. (2009) 176, 164–174 doi: 10.1111/j.1365-246X.2008.03966.x.

Priestley, K and J. Brune, 1978. Surface waves and the structure of the Great Basin of Nevada and western Utah, JGR, v. 83, pp. 2265-2272.

Sanchez-Sesma, F. J., and M. Campillo, 2006. Retrieval of the Green's function from cross correlation: The canonical elastic problem. *Bull. Seism. Soc. Am.*, 96, 1182-1191, doi: 10.1785/0120050181.

Sabra, K. G., P. Gerstoft, P. Roux, W. A. Kuperman, and M. C. Fehler, 2005. Surface wave tomography from microseisms in southern California, Geophys. Res. Lett., 32, L14311, doi:10.1029/2005GL023155.Sanchez-Sesma and Campillo, 2006

Scott, J. B., M. Clark, T. Rennie, A. Pancha, H. Park and J. N. Louie, 2004, A shallow shear-wave velocity transect across the Reno, Nevada area basin, Bull. Seism. Soc. Am. 94, no. 6, 2222-2228.

Shapiro, N. M., Campillo, M., Stehly, L., and Ritzwoller, M. H., 2005. High-resolution surface wave tomography from ambient seismic noise, *Science*, 307, 1615-1618.

Stoica, P., and R. Moses. Introduction to Spectral Analysis. Upper Saddle River, NJ: Prentice-Hall, 1997. Pgs. 61-64.

Tibuleac, I. M. and Herrin, E, 1997. Calibration Studies at TXAR, Seis. Res. Lett. **68**, 353-365.

Tibuleac, I.M., and E.T. Herrin, 1999. An automatic method for determination of Lg arrival time using wavelet transforms, Seism. Res. Lett. 70, 577-595

Tibuleac, I. and J. Britton, 2006. An Automated Short-Period Surface-Wave Detection Algorithm, Bull. Seis. Soc. Am. 96, 334-343

Tsai, V. C., 2009. On establishing the accuracy of noise tomography travel-time measurements in a realistic medium, *Geophys. J. Int.* 178, 1555–1564

Yang, Y., M.H. Ritzwoller, F.-C. Lin, M.P. Moschetti, and N.M. Shapiro, 2008.The structure of the crust and uppermost mantle beneath the western US revealed by ambient noise and earthquake tomography, J. Geophys. Res., 113, B12310, doi:10.1029/2008JB005833, 2008

Yao, H., R. D. van der Hilst and M. V. de Hoop, 2006. Surface-wave array tomography in SE Tibet from ambient seismic noise and two-station analysis – I. Phase velocity maps, Geophys. J. Int. (2006),166, 732–744

Yao, H., Beghein, C., and Van der Hist, R.D., 2008. Surface-wave array tomography in SE Tibet from ambient seismic noise and two-station analysis: II – Crustal and upper-mantle structure, Geophys. J. Int., Vol. 163, 205-219, doi: 10.1111/j.1365-246X.2007.03696.x.

Wapenaar, K., 2004. Retrieving the elastodynamic Green's function of an arbitrary inhomogeneous medium by cross-correlation: Physical Review Letters, 93, 254301.

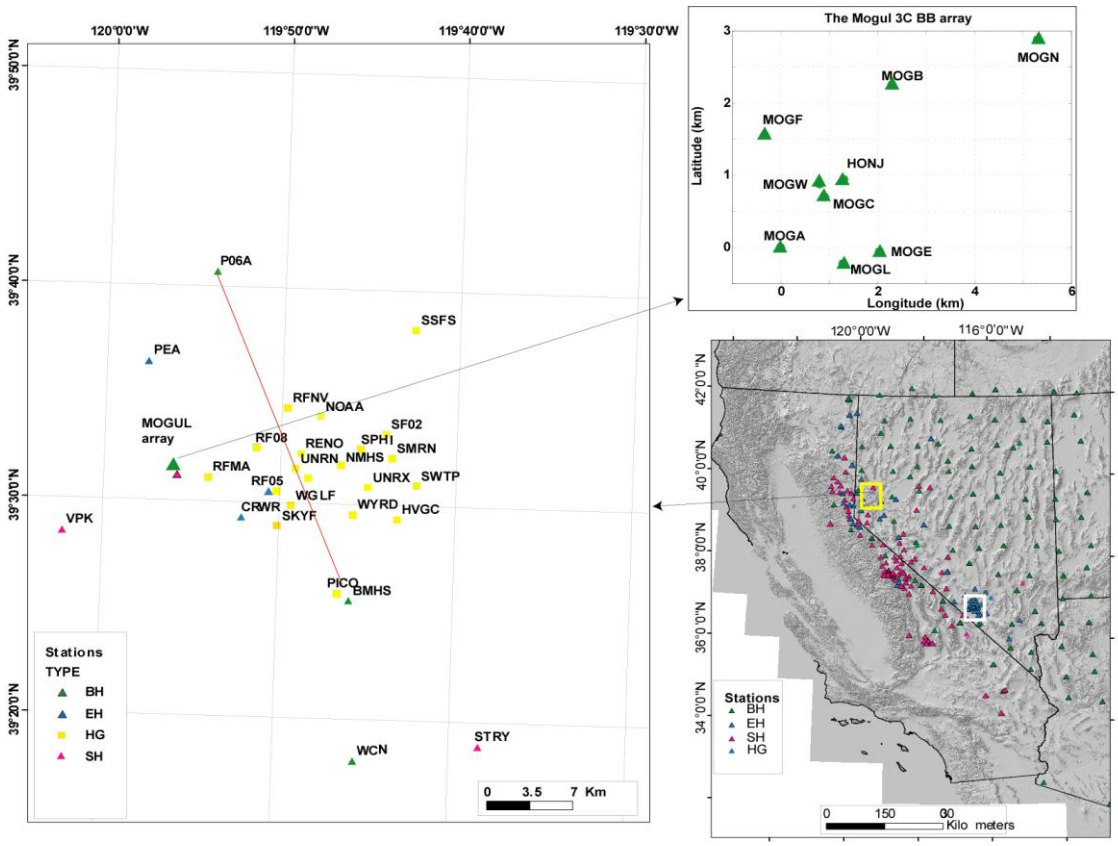

Figure 1. Left plot: The Reno Basin station locations (BH - broadband sensors are shown as green triangles, EH - short period sensors are shown as blue triangles, SH - analog short period sensors are shown as magenta triangles and HG - accelerometers are shown by yellow squares). The upper right plot shows the 2008 Mogul RAMP deployment of broadband sensors in Mogul, west of Reno. The lower right plot shows the network of instruments with continuous records available at the Nevada Seismological Laboratory. The green triangles show locations of the 3C broadband sensors of the Transportable Array EarthScope 2006-2008 deployment. The sensors are shown with the same color code as in the left plot. The yellow and white rectangles in the lower right plot show the Reno Basin area (in the left plot) and the Southern Great Basin Seismic Network area. A red line on the left map shows a path from BH station P06A to HG accelerometer PICO, which is ~ 1 km from BH sensor BMHS.

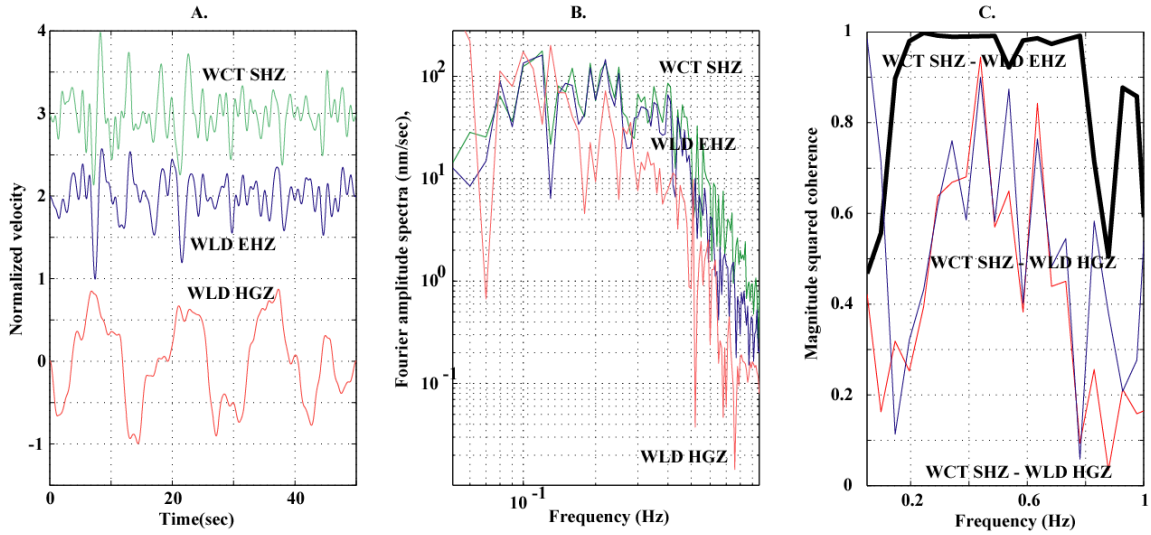

Figure 2. Recordings at co-located instruments at Wildcat Mountain (36.79 N, 116.62 W), near Yucca Mountain, Nevada. Plot A shows the normalized traces after being reshaped to a BH instrument with corner frequency 0.1 Hz and after being filtered with a zero-phase, four pole Butterworth filter, from 0.05 to 1 Hz. The sensors are WLD:EHZ (EH), a narrow-band digital seismometer (S-13), WCT:SHZ (SH), a narrow-band analog seismometer (L-4), and WLD:HGZ (HG), a digital accelerometer (131A_02 MEMS). Plot B shows the Fourier amplitude spectrum (nm/s) in the band of interest for the HG (red), EH (blue) and SH (green) vertical components, after being reshaped to a BH instrument with corner frequency 0.1 Hz. Note the lack of similarity of the HG spectra to the EH and SH spectra at all frequencies. Plot C shows the magnitude squared coherence (with a maximum value of 1) for pairs of sensors in the frequency band of interest. While the short-period sensor recordings (WCT SH and WLD EH, shown in black) are coherent at frequencies lower than 1 Hz, the accelerometer noise and the noise recorded by the short-period instruments (blue and red) are not coherent at frequencies below 1 Hz.

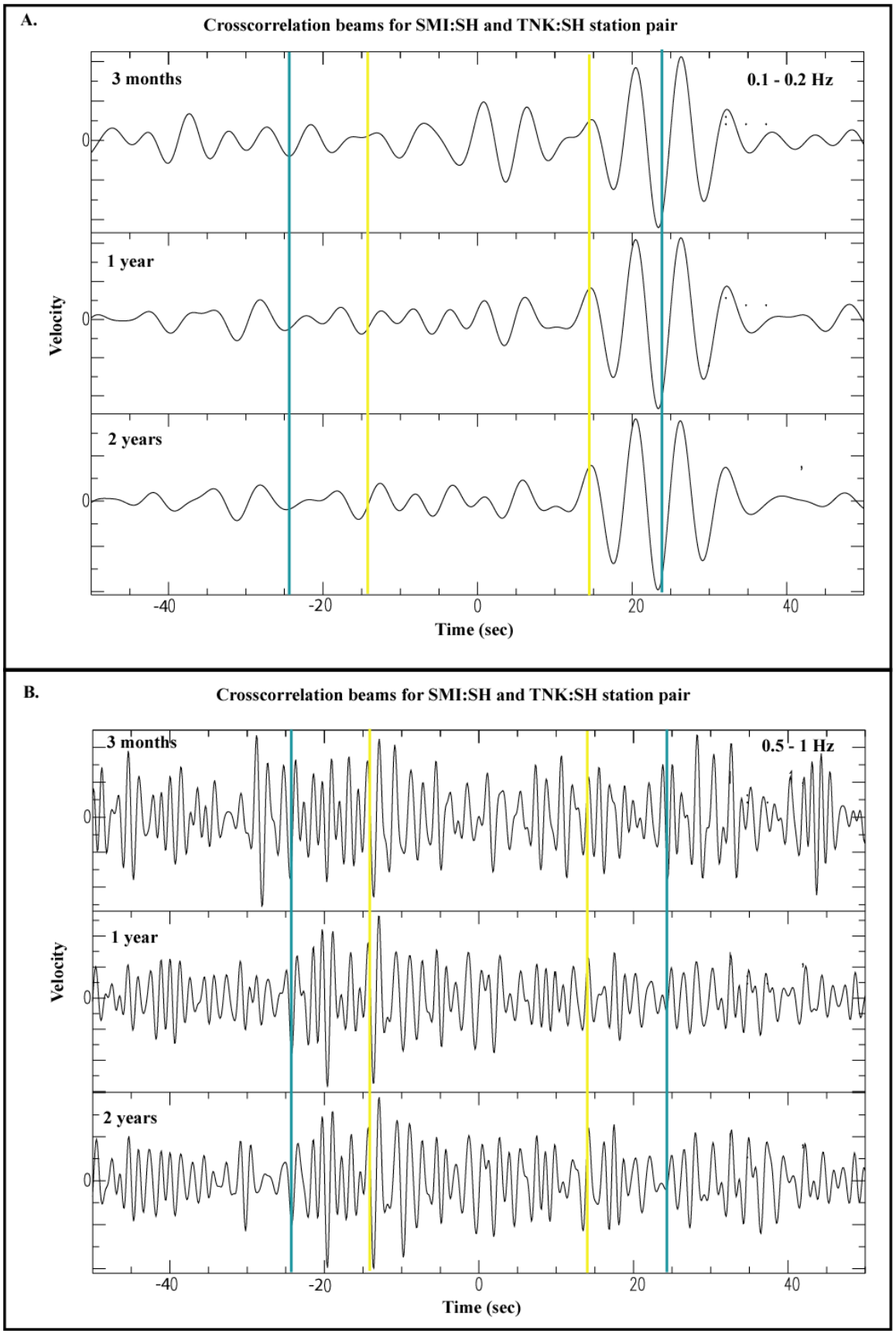
A.
Crosscorrelation beams for SMI:SH and TNK:SH station pair
3 months
0.1 - 0.2 Hz
1 year
2 years
Velocity
0
-40
-20
0
20
40
Time (sec)
B.
Crosscorrelation beams for SMI:SH and TNK:SH station pair
3 months
0.5 - 1 Hz
1 year
2 years
Velocity
0
-40
-20
0
20
40
Time (sec)

Figure 3. GF extraction for analog sensor pairs (Table 4) is possible for a 3-month period, however, a longer analysis time length (~ 1 year) is recommended for GF extraction. Waveforms resulting from cross-correlation stacks at SMI and TNK are shown for two different frequency bands in insets A and B. Inset A shows two-sided cross-correlation stacks for an analysis period of 3 months, one year and two years. The waveforms are filtered from 0.1 to 0.2 Hz, with a three-pole, zero phase Butterworth filter. The blue lines at ±23.6 s time lag show the expected arrival time of a 3 km/s Rayleigh phase. Note the cross-correlation beam asymmetry in the upper plots. Also, note the Rayleigh wave emerging from the noise for the three-month stack, and becoming better defined for the one year stack. The one year and two-years stacks are very similar, thus, analysis of one year of data is sufficient for a well-defined GF function. The yellow lines show the expected arrival time of a 5 km/s Pg phase (±14.3 s) from a distance of 71.3 km. We interpret the higher frequency (0.5 - 1 Hz), arrivals emerging from noise at ~14 s time lag in inset B as low signal-to-noise (SNR) crustal first P arrivals. Note the presence of these arrivals on the opposite side of the cross-correlation trace from the Rayleigh wave-dominated GF.

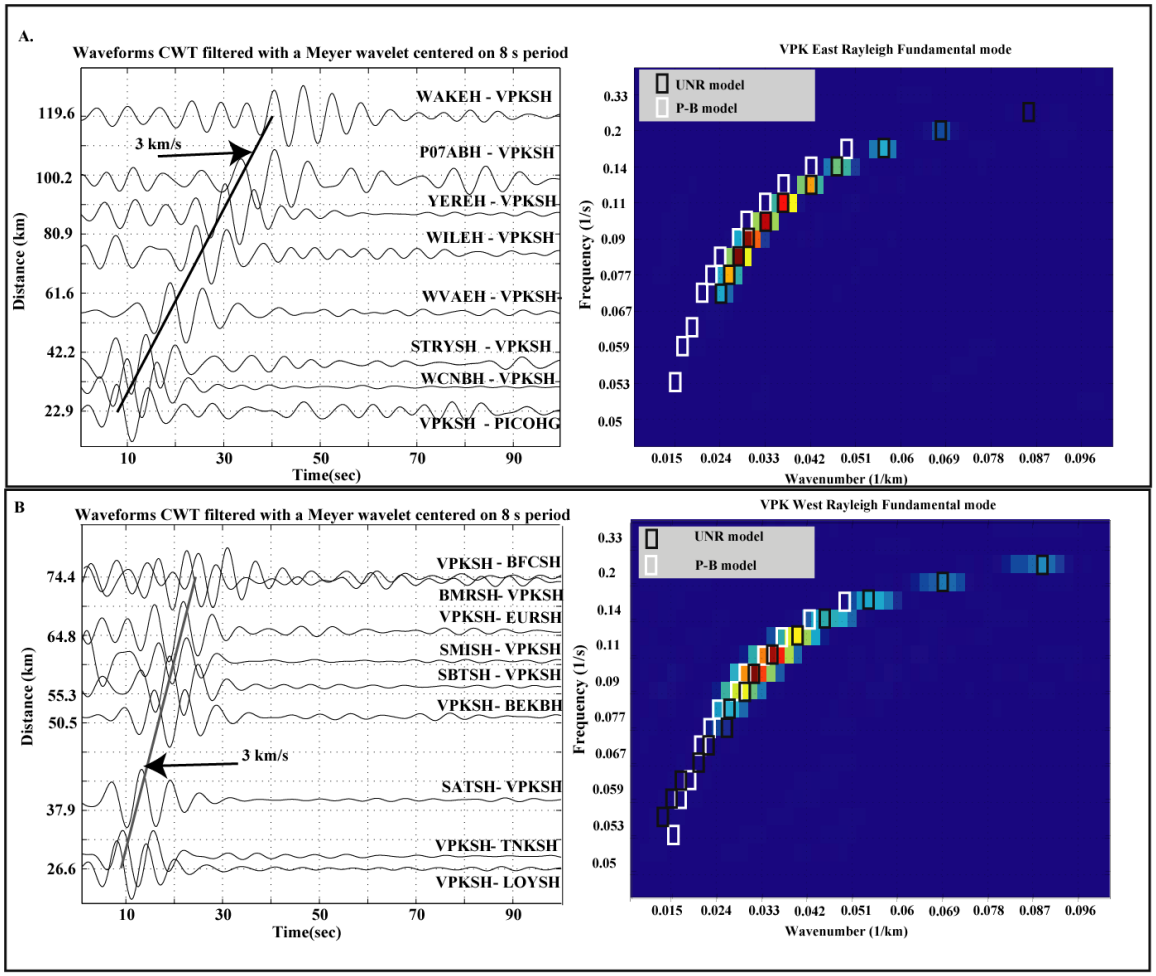

Figure 4. Left plots show record sections of recovered GF's (scaled to their maximum value) after being filtered using a Meyer wavelet centered on 8 s period. All station pairs include an analog seismometer at station VPK. The FK analysis for these record sections

is shown in the right plots. The black rectangles on the FK plots show the peak FK amplitude for each wavenumber. The region sampled in Figure 4A includes the Reno-Carson City basins, east of VPK, and is characterized by lower phase velocity than predicted by the Priestley and Brune (1978) model (P-B model). The region sampled in Figure 4B is in the northern Sierra Nevada, west of VPK, and the estimated phase velocity dispersion curve is faster than the curve predicted by the P-B model. Station locations are listed in Table 4. The black line in each of the left plots shows the 3 km/s arrival time lag for the Rayleigh phases. In the right plots, the reference dispersion curves are represented by open white rectangles and show the fundamental (FR) dispersion curves estimated using the P-B model. The open black rectangles mark the largest amplitude value in each FK plot.

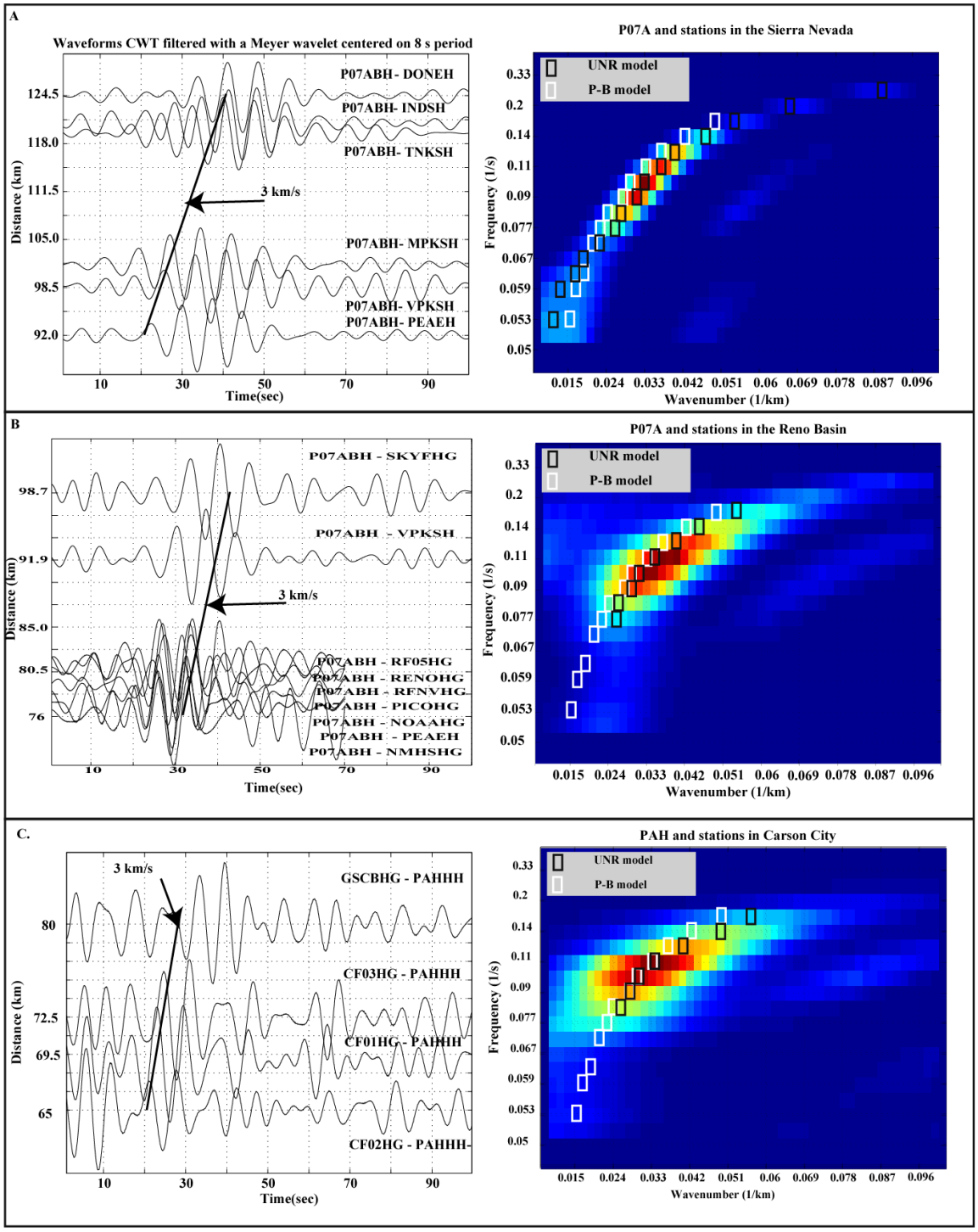

Figure 5. The insets A-C show retrieval of GF's from broadband (BH and HH) sensors paired with EH, SH, and HG sensors. Waveforms are filtered using a Continuous Wavelet Transform with a Meyer wavelet centered on 8 s period. Each waveform is scaled to its maximum value. The left plots show GF record sections for pairs of stations including the P07A BH (A and B) and PAH BH (C). The right plots show the FK analysis of the record sections. Note lower Rayleigh phase velocity values in the Reno-Carson City area when compared to the reference dispersion curve (open black rectangles) from

Priestley and Brune (1978). The black line in the left plot shows the time lags for 3 km/s phases. The encircled areas on the FK plots show the range of values we use for phase-velocity estimation. The black open square marks the largest amplitude value in each FK plot.

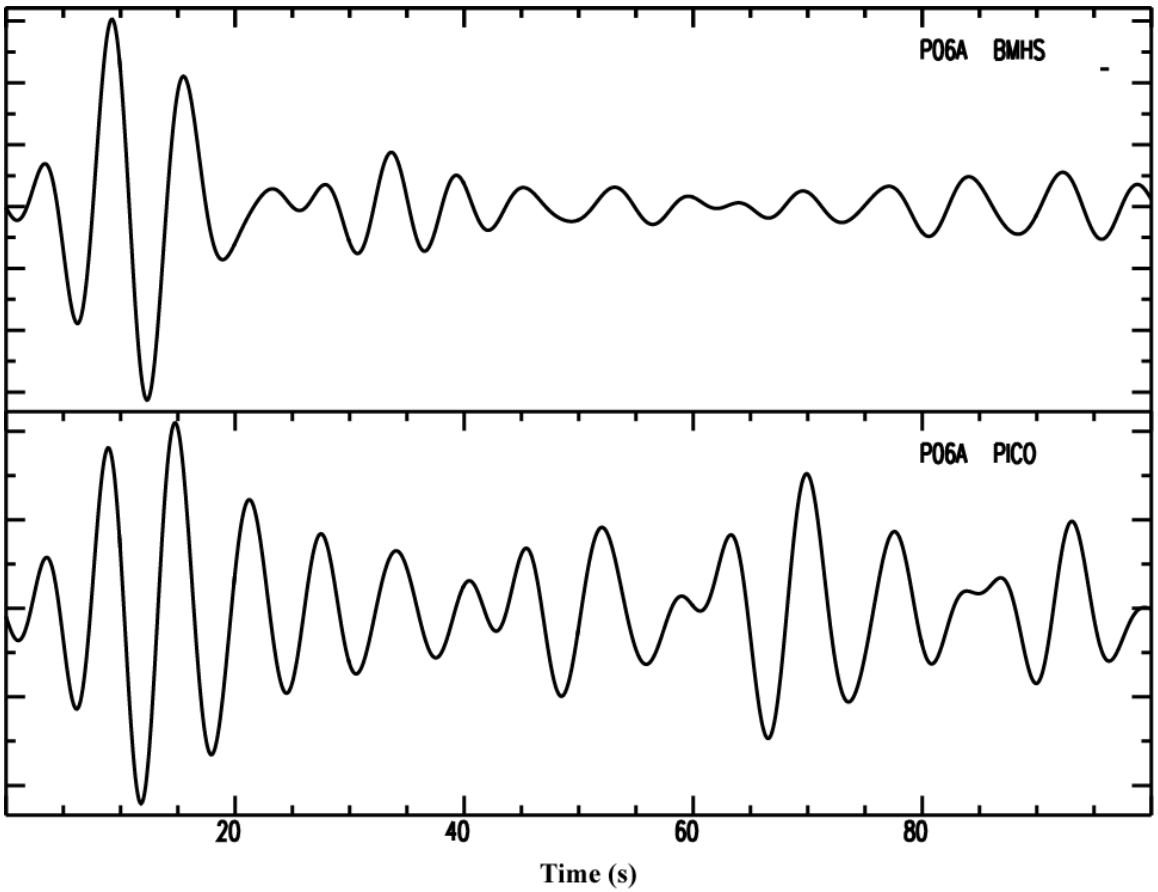

Figure 6. Similar shape GF's are extracted on the vertical components for the P06A BHZ - BMHS BHZ pair (upper plot) and the P06A BHZ -PICO HGZ pair (lower plot), indicating that similar GF's are retrieved at 5-10 s periods from different sensors (broadband velocity sensor and accelerometer). The waveforms are filtered from 0.1 to 0.2 Hz, with a Butterworth, four-pole, zero-phase filter, Velocity is scaled to the absolute maximum value, and each vertical axis ranges from 1 to -1. The time length for stacking was two years. Stations PICO and BMHS are ~ 1 km apart.

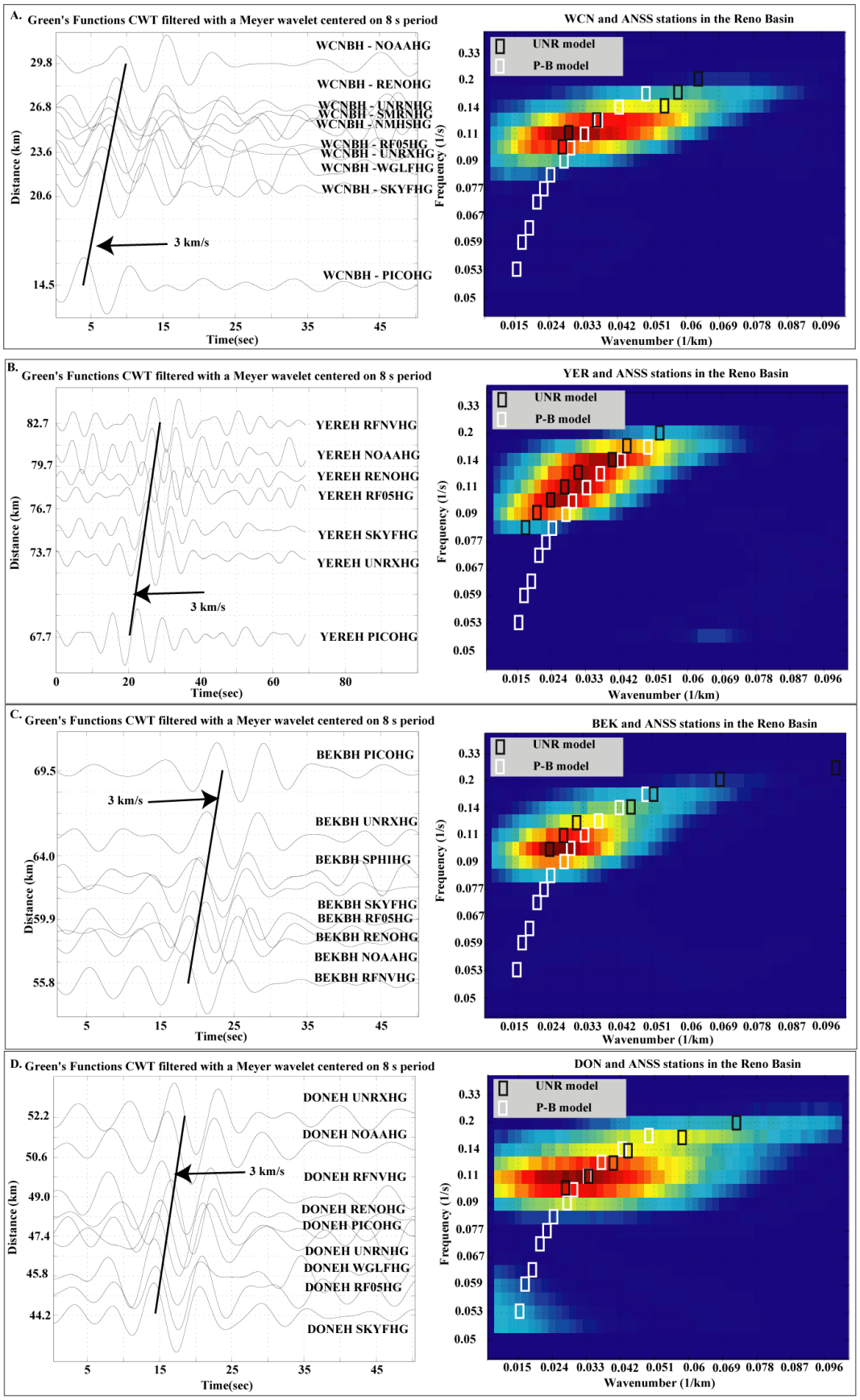
A.
Green's Functions CWT filtered with a Meyer wavelet centered on 8 s period
WCN and ANSS stations in the Reno Basin
WCNBH - NOAAHG
WCNBH - RENOHG
WCNBH - UNRNHG
WCNBH - SMRNHG
WCNBH - NMHSHG
WCNBH - RF05HG
WCNBH - UNRXHG
WCNBH -WGLFHG
WCNBH - SKYFHG
WCNBH - PICOHG
3 km/s
Distance (km)
Time(sec)
UNR model
P-B model
Frequency (1/s)
Wavenumber (1/km)
B.
Green's Functions CWT filtered with a Meyer wavelet centered on 8 s period
YER and ANSS stations in the Reno Basin
YEREH RFNVHG
YEREH NOAAHG
YEREH RENOHG
YEREH RF05HG
YEREH SKYFHG
YEREH UNRXHG
YEREH PICOHG
3 km/s
Distance (km)
Time(sec)
UNR model
P-B model
Frequency (1/s)
Wavenumber (1/km)
C.
Green's Functions CWT filtered with a Meyer wavelet centered on 8 s period
BEK and ANSS stations in the Reno Basin
BEKBH PICOHG
BEKBH UNRXHG
BEKBH SPHIHG
BEKBH SKYFHG
BEKBH RF05HG
BEKBH RENOHG
BEKBH NOAAHG
BEKBH RFNVHG
3 km/s
Distance (km)
Time(sec)
UNR model
P-B model
Frequency (1/s)
Wavenumber (1/km)
D.
Green's Functions CWT filtered with a Meyer wavelet centered on 8 s period
DON and ANSS stations in the Reno Basin
DONEH UNRXHG
DONEH NOAAHG
DONEH RFNVHG
DONEH RENOHG
DONEH PICOHG
DONEH UNRNHG
DONEH WGLFHG
DONEH RF05HG
DONEH SKYFHG
3 km/s
Distance (km)
Time(sec)
UNR model
P-B model
Frequency (1/s)
Wavenumber (1/km)

Figure 7. Phase-velocity was extracted beneath adhoc combinations of stations within the ANSS array in the Reno Basin, for paths from these stations to a station in the Reno-Carson City area. Left plots in A-D show the GF's we have estimated from ambient noise, scaled to the maximum value. The right plots show the phase velocity estimated at each adhoc array. Waveforms are filtered using a Continuous Wavelet Transform with a Meyer wavelet centered on 7 or 8 s period as indicated on the plot. The reference dispersion curve (white open rectangles) in the right plots is from Priestley and Brune (1978). The open black rectangles on the FK plots show the maximum FK value for each wave number.

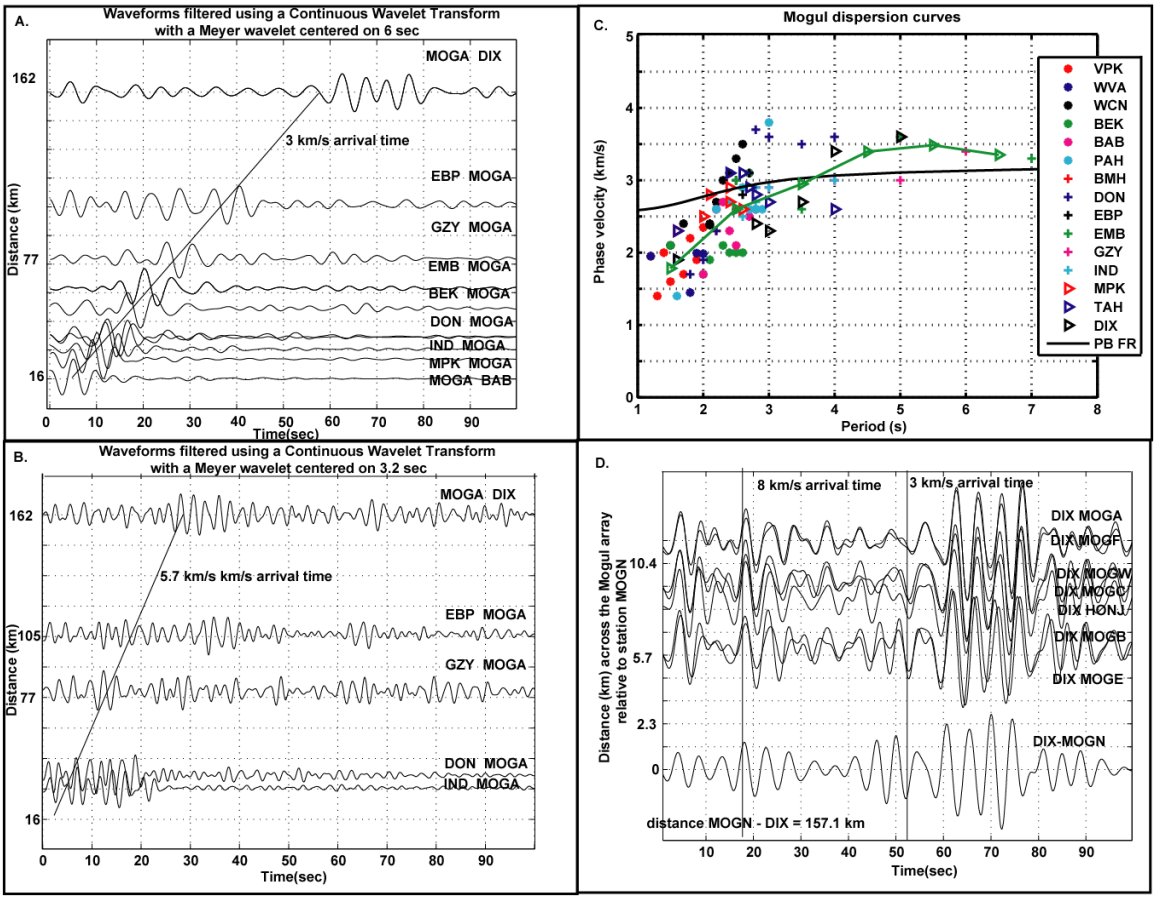

Figure 8 shows examples of the GF analysis at the Mogul array. The left plots show GF's extracted for paths from a Mogul station (MOGA) to stations in the Reno Basin. Fundamental mode Rayleigh waves are shown in Figure 8A. Figure 8B shows the same waveforms filtered in a higher frequency band and arrivals with 5.7 km/s group velocity which we interpret as Pg-waves. All the arrivals interpreted as P in this plot were also identified (using back azimuth and horizontal velocity) on Mogul array beams, using crosscorrelation in time domain (Table 1). The upper right plot shows Rayleigh phase velocity dispersion curves resulted from applying time-domain crosscorrelation (Tibuleac and Herrin, 1997) to GF's extracted for paths from Nevada Network seismic stations and adhoc combinations of stations within the Mogul array (Figure8C). The reference dispersion curve (black line - model PB FR) in the right upper plot is from Priestley and

Brune (1978). The green triangles and the green line Figure 8C show the median value of the fundamental Rayleigh (FR) phase velocity in 1 s bins. We linearly interpolate the median values for the missing periods. Figure 8D shows an example of the GF's extracted for paths from DIX to Mogul stations using a Continuous Wavelet Transform with a Meyer wavelet centered on 2.5 s period. These waveforms are analyzed to obtain the right open triangles corresponding to the DIX station in Figure 8C. A large arrival at 18 s time lag with 8 km/s group velocity is interpreted at Pn. The use of wavelet-based filters and "illumination" of the entire area by the Mogul sequence in 2008 are possible causes for P-arrival observations in insets B and D. Note, however, the low SNR of these P-arrivals.

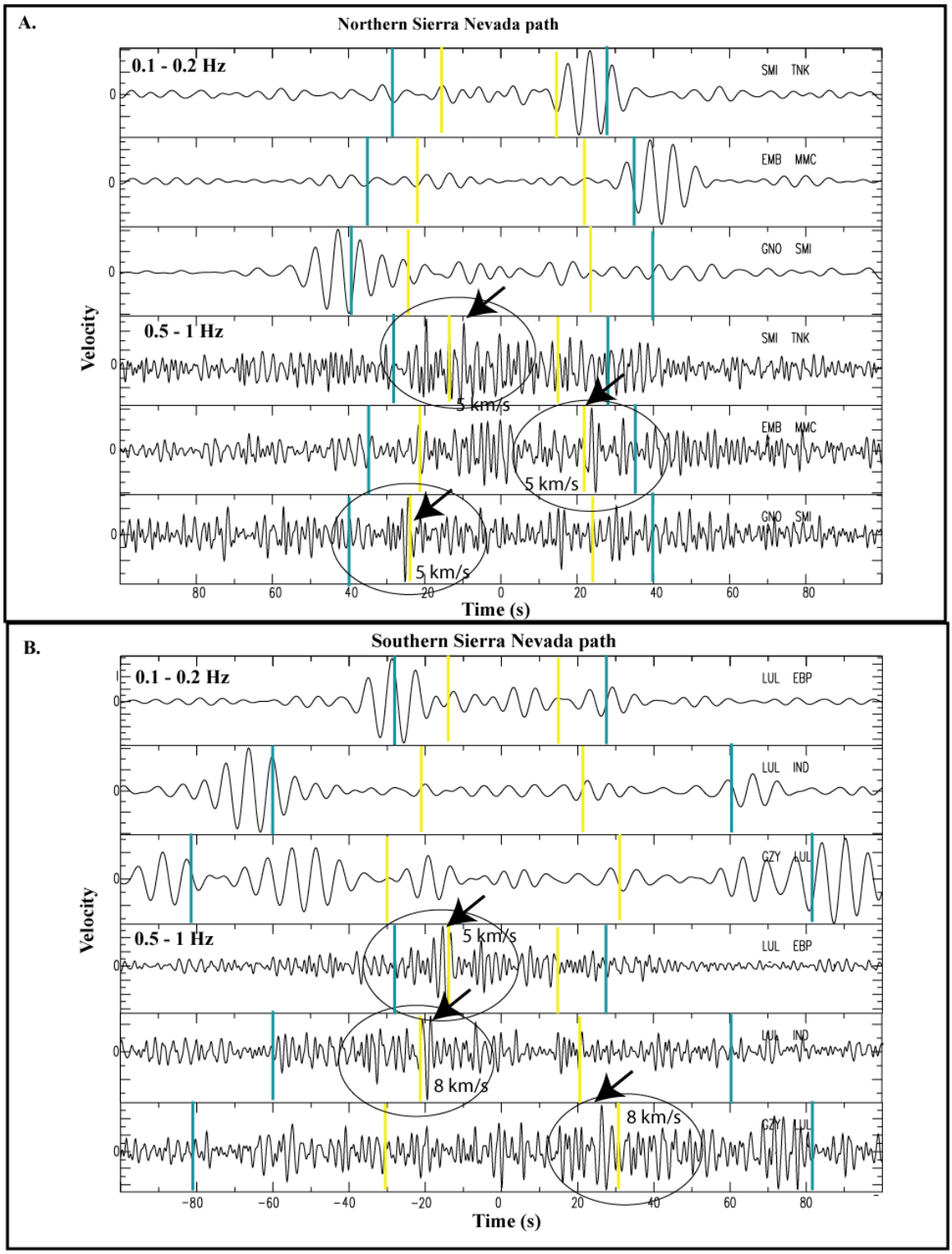

Figure 9. GF extraction for pairs of analog sensors for stations in the northern (upper set of plots) and southern (lower set of plots) Sierra Nevada Range. All GF's are scaled to the absolute value of the maximum amplitude. The dominant, Rayleigh wave GF component (0.1 - 0.2 Hz) is shown in the upper three plots of each inset. The largest short-period arrivals in the lower three plots of each inset are interpreted as the P phase

of the Green's function. The P phase is identified on the same side with the visible Rayleigh GF for all station pairs except SMI-TNK (see also Figure 3). Time lags for the blue lines are estimated using the inter-station distances in Table 4 and 3 km/s Rayleigh velocity. Time lags for the yellow lines are estimated using the inter-station distances in Table 4 and 6 km/s Pg velocity at distances < 150 km, or 8 km/s Pn velocity for stations > 150 km (i.e. for the station pairs GZY-LUL and LUL - IND).

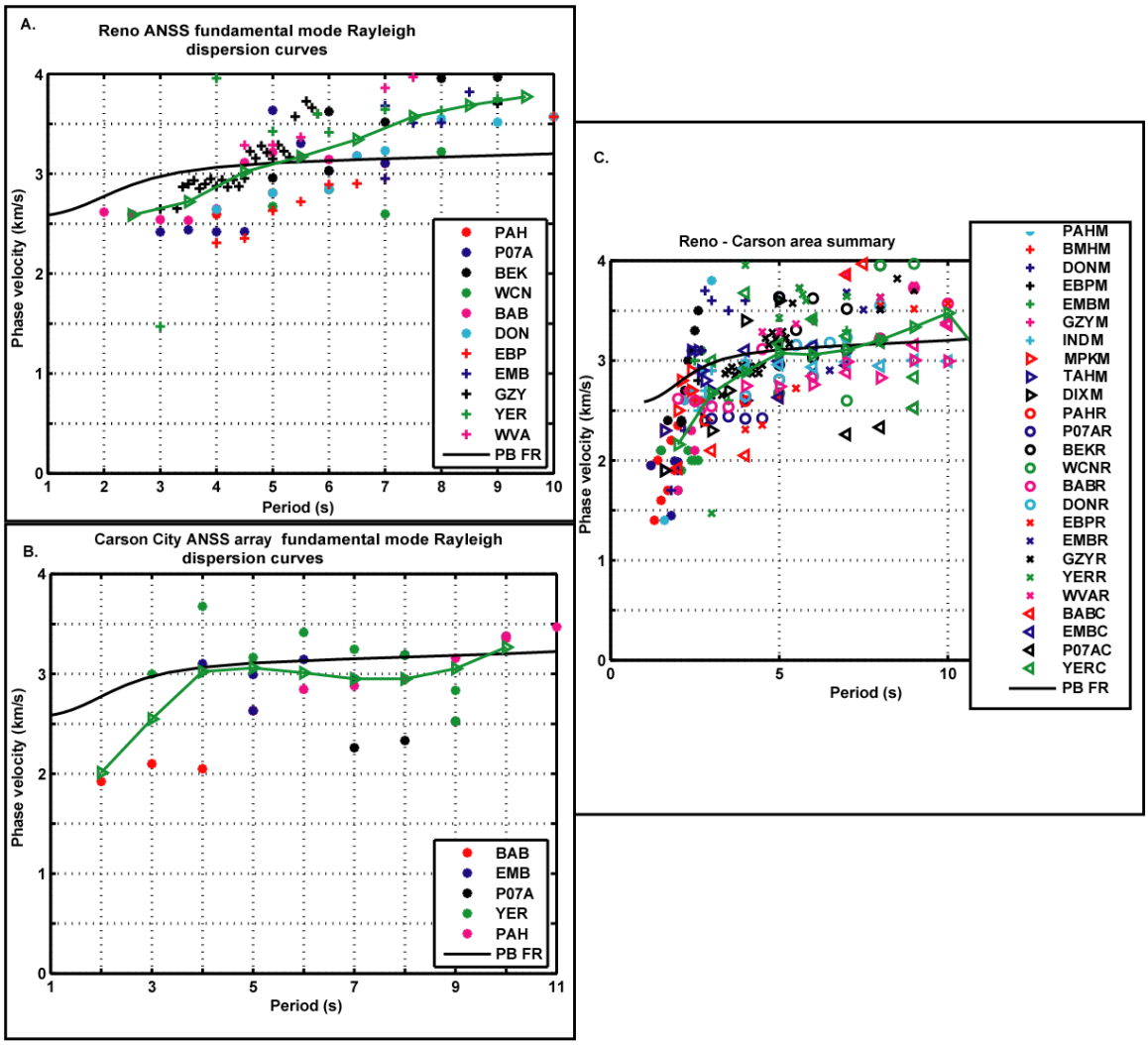

Figure 10A shows fundamental mode Rayleigh phase velocity estimates beneath the ANSS array in Reno, extracted from pairs of stations shown in Figure 7 and listed in Table 4. Figure 10B shows phase velocity beneath the ANSS array in Carson City, NV, extracted from pairs of stations listed in Table 4. Figure 10C shows a summary of phase velocities (see also Table 1) estimated for all the adhoc arrays in the Reno-Carson City area. The green triangles and the green line in each plot show the median value of the fundamental Rayleigh (FR) phase velocity in 1 s bins. We linearly interpolate the median values for the missing periods. Fundamental mode Rayleigh phase velocity dispersion measurements for each virtual source (i.e. Nevada Network station) are marked by the symbols shown in the legend. The black curves in each plot show the phase velocity

calculated from the Priestley and Brune (1978) model for fundamental mode Rayleigh (PB FR).

Table 1. Results of crosscorrelation in time domain applied to P-arrival windows at the Mogul array. The waveforms are filtered using a Continuous Wavelet Transform centered on a period shown in the fifth column. Since P was usually observed at more than one center period, the sixth column shows the period range in which P -arrivals were identified.

1.Virtual source	2.Horizontal velocity (km/s)	3. Estimated back-azimuth (deg)	4. "True" back azimuth (deg)	5.Meyer wavelet center period (s)	6.Period range (s) for P arrival observations
DIX	5.7	53	79	2.4	2.1 - 3
DON	5.5	228	219	2.4	2.4 - 3
EBP	6.8	180	173	2.6	2.1-2.6
GZY	6.5	306	309	2.4	2.2 - 2.4
IND	5.4	271	251	2.4	2.2 - 3

Table 2. Phase velocity dispersion curves extracted in Figure 10.

MOGUL BROADBAND ARRAY		ANSS RENO ACCELEROMETER NETWORK		ANSS CARSON ACCELEROMETER ARRAY		*RENO-CARSON AREA SUMMARY*	
Period (s)	Phase velocity (km/s)	Period (s)	Phase velocity (km/s)	Period (s)	Phase velocity (km/s)	Period (s)	Phase velocity (km/s)
1.5	1.78	2.5	2.6	2	1.92	1.5	1.85
2.5	2.6	3.5	2.7	3.0	2.54	2	2.1
3.5	2.95	4.5	3.0	4	3.1	3	2.7
5.5	3.5	5.5	3.2	5	3	4	2.9
6.5	3.3	6.5	3.3	6	3.1	5	3.1
		7.5	3.6	7	2.9	6	3.1
		8,5	3.7	*10*	*3.4*	7	3.1
		9,5	3.8			8	3.2
						9	3.3
						10	3.5

Table 3. Shear velocity models extracted from the dispersion curves in Table 2 and Figure 10.

Location	Mogul array estimated model	ANSS array Reno estimated model	ANSS array Carson estimated model	Reno-Carson area estimated model	Starting model
Layer thickness (km)	Shear velocity (km/s)	Shear velocity (km/s)	Shear velocity (km/s)	Shear velocity (km/s)	Shear velocity (km/s)
1	1.6		1.7	1.7	2.2
1	2.5		2.0	2.2	2.2
2	3.5	2.8	3.4	3.4	2.5
2	4.0	3.7	3.8	3.7	2.9
2	4.5	4.4	3.9	4.0	3.6

Table 4.Inter-station distance and station location for station pairs in Figures 3-10.

Station 1	Station 2	Distance (km)	Back Azimuth (deg)	Lat. Station 1 (deg)	Lon Station 1 (deg)	Lat. Station 2 (deg)	Lon. Station 2 (deg)
Figure 3							
SMI	TNK	71.2	339	39.8673	-120.5295	39.2675	-120.2358
Figure 4A							
STRY	VPK	38.5	117	39.3151	-119.6386	39.4747	-120.0373
VPK	PICO	22.9	282	39.4747	-120.0373	39.4312	-119.7756
WAK	VPK	119.7	154	38.5044	-119.4372	39.4747	-120.0373
WCN	VPK	30.8	128	39.3017	-119.7563	39.4747	-120.0373
WIL	VPK	74.6	171	38.8104	-119.9083	39.4747	-120.0373
WVA	VPK	55.3	19	39.9445	-119.8240	39.4747	-120.0373
YER	VPK	87.6	128	38.9845	-119.2407	39.4747	-120.0373
P07A	VPK	98.7	85.4	39.5399	-118.8893	39.4747	-120.0373
Figure 4B							
BEK	VPK	51.5	327.8	39.8667	-120.3586	39.4747	-120.0373
BFC	VPK	74.4	150.0	38.8940	-119.6077	39.4747	-120.0373
BMR	VPK	73.7	342.9	40.1087	-120.2910	39.4747	-120.0373
EUR	VPK	65.5	298.5	39.7542	-120.7108	39.4747	-120.0373
TNK	VPK	28.6	216.5	39.2675	-120.2358	39.4747	-120.0373
VPK	LOY	26.6	140.1	39.4747	-120.0373	39.6587	-120.2358
SMI	VPK	60.6	316	39.8673	-120.5295	39.4747	-120.0373
SBT	VPK	56.4	287	39.5268	-120.6658	39.4747	-120.0373
SAT	VPK	37.8	292	39.6025	-120.4470	39.4747	-120.0373
Figure 5A							
P07A	PEA	92	94	39.5399	-118.8893	39.6076	-119.9600
P07A	DON	124.6	79.8	39.5399	-118.8893	39.3517	-120.3205
P07A	IND	120.9	83.9	39.5399	-118.8893	39.4343	-120.2917

P07A	MPK	101.6	74.1	39.5399	-118.8893	39.2957	-120.0302
P07A	TNK	119.5	74.9	39.5399	-118.8893	39.2675	-120.2358
P07A	VPK	98.7	85.4	39.5399	-118.8893	39.4747	-120.0373
Figure 5B							
PAH	CF01	69.06	28.1	39.7065	-119.3842	39.1593	-119.7647
PAH	CF02	65.05	28.0	39.7065	-119.3842	39.1907	-119.7418
PAH	CF03	72.49	26.8	39.7065	-119.3842	39.1257	-119.7676
PAH	GSCB	80.1	28	39.7065	-119.3842	39.2267	-120.0812
Figure 6							
P06A	BMHS	30.3	157.7	39.6785	-119.8983	39.4257	-119.9764
P06A	PICO	29.4	158.9	39.6785	-119.8983	39.4312	-119.7756
Figure 7A							
WCN	NMHS	25.5	176	39.3017	-119.7563	39.5309	-119.7754
WCN	NOAA	29.8	173	39.3017	-119.7563	39.5681	-119.7958
WCN	RENO	26.8	169	39.3017	-119.7563	39.5391	-119.8138
WCN	RF05	24	163	39.3017	-119.7563	39.5094	-119.836
WCN	SKYF	21.1	161	39.3017	-119.7563	39.4825	-119.8340
WCN	UNRN	25.6	168	39.3017	-119.7563	39.527	-119.818
WCN	UNRX	23.6	181	39.3017	-119.7563	39.5141	-119.7493
WCN	WGLF	22.6	165	39.3017	-119.7563	39.4986	-119.8216
WCN	PICO	14.4	173.4	39.3017	-119.7563	39.4312	-119.7756
WCN	SMRN	26.3	185	39.3017	-119.7563	39.5372	-119.7274
Figure 7B							
YER	PICO	67.7	137	38.9845	-119.2407	39.4312	-119.7756
YER	RENO	79	141	38.9845	-119.2407	39.5391	-119.8138
YER	RFNV	82.7	142	38.9845	-119.2407	39.5742	-119.8275
YER	RF05	77.6	138	38.9845	-119.2407	39.5094	-119.836
YER	SKYF	75.3	137	38.9845	-119.2407	39.4825	-119.8340
YER	UNRX	73.4	143	38.9845	-119.2407	39.5141	-119.7493
YER	NOAA	80.6	143	38.9845	-119.2407	39.7065	-119.3842
Figure 7C							
BEK	NOAA	58.4	304.7	39.8667	-120.3586	39.5681	-119.7958
BEK	PICO	69.5	314.3	39.8667	-120.3586	39.4312	-119.7756
BEK	RENO	59.1	308.1	39.8667	-120.3586	39.5391	-119.8138
BEK	RF05	59.8	311.8	39.8667	-120.3586	39.5094	-119.836
BEK	RFNV	55.9	305.7	39.8667	-120.3586	39.5742	-119.8275
BEK	UNRN	59.7	309.4	39.8667	-120.3586	39.527	-119.818
BEK	UNRX	65.2	307.1	39.8667	-120.3586	39.5141	-119.7493
BEK	PICO	69.6	314.3	39.8667	-120.3586	39.4312	-119.7756
Figure 7D							
DON	WGLF	45.8	249.2	39.3517	-120.3205	39.4986	-119.8216
DON	RF05	45.1	247.3	39.3517	-120.3205	39.5094	-119.836
DON	NOAA	51.0	242.0	39.3517	-120.3205	39.5681	-119.7958
DON	PICO	47.6	259.4	39.3517	-120.3205	39.4312	-119.7756
DON	RENO	48.2	244.5	39.3517	-120.3205	39.539	-119.8138
DON	RFNV	49.0	239.8	39.3517	-120.3205	39.5742	-119.8275

DON	SKYF	44.2	250.9	39.3517	-120.3205	39.4825	-119.8340
DON	UNRN	47.3	245.8	39.3517	-120.3205	39.527	-119.81
DON	UNRX	52.2	249.9	39.3517	-120.3205	39.5141	-119.7493
Figure 8A,B and C, Table 2							
MOGA	DIX	162.5	79	39.5517	-119.9216	39.8022	-118.0820
MOGA	EBP	105.1	173	39.5517	-119.9216	38.5828	-119.8063
MOGA	GZY	77.6	309	39.5517	-119.9216	39.9620	-120.6502
MOGA	DON	37.3	219	39.5517	-119.9216	39.3517	-120.3205
MOGA	IND	31.2	251	39.5517	-119.9216	39.4343	-120.2917
Figure 9							
SMI	TNK	71.2	339	39.8673	-120.5295	39.2675	-120.2358
EMB	MMC	108.6	309	38.9748	-120.1019	38.3608	-119.1283
GNO	SMI	119.4	150	38.9292	-119.8528	39.8673	-120.5295
GZY	LUL	247.4	329	39.9620	-120.6502	38.0523	-119.1803
LUL	EBP	80.3	137	38.0523	-119.1803	38.5828	-119.8063
LUL	IND	181.3	147	38.0523	-119.1803	39.4343	-120.2917
Other groups of stations used in this study, and not illustrated in the figures, however used in Figure 10							
HONJ	BAB	16.83904	117.73120	39.5307	-119.9302	39.6013	-120.1040
MOGA	BAB	16.19217	122.84929	39.5222	-119.9454	39.6013	-120.1040
BAB	MOGB	17.18273	292.42349	39.6013	-120.1040	39.5425	-119.9186
BAB	MOGC	16.60927	299.22082	39.6013	-120.1040	39.5285	-119.9348
MOGE	BAB	17.96	109.37476	39.5217	-119.9216	39.6013	-120.1040
BAB	MOGF	15.11426	298.66394	39.6013	-120.1040	39.5362	-119.9492
BAB	MOGN	19.79385	287.45847	39.6013	-120.1040	39.5481	-119.8836
MOGW	BAB	16.43294	118.74685	39.5301	-119.9360	39.6013	-120.1040
BAB	RENO	25.81670	285.63110	39.6013	-120.1040	39.5391	-119.8138
NMHS	BAB	29.23352	105.42673	39.5309	-119.7754	39.6013	-120.1040
NOAA	BAB	26.66709	97.85875	39.5681	-119.7958	39.6013	-120.1040
PICO	BAB	33.92955	123.77379	39.4312	-119.7756	39.6013	-120.1040
RFNV	BAB	23.88371	97.15983	39.5742	-119.8275	39.6013	-120.1040
SKYF	BAB	26.65454	119.62177	39.4825	-119.8340	39.6013	-120.1040
SMRN	BAB	33.05638	102.33130	39.5372	-119.7274	39.6013	-120.1040
SPHI	BAB	30.39946	102.07314	39.5436	-119.7573	39.6013	-120.1040
SWTP	BAB	35.60669	105.24645	39.5164	-119.7035	39.6013	-120.1040
UNRX	BAB	31.91529	107.57279	39.5141	-119.7493	39.6013	-120.1040
GZY	HONJ	78.02984	308.15151	39.9620	-120.6502	39.5307	-119.9302
GZY	MOGA	77.60386	309.28512	39.9620	-120.6502	39.5222	-119.9454
GZY	MOGB	78.01882	306.94989	39.9620	-120.6502	39.5425	-119.9186
GZY	MOGC	77.87193	308.46940	39.9620	-120.6502	39.5285	-119.9348
GZY	MOGE	77.22	306.45602	39.9620	-120.6502	39.5217	-119.9216
GZY	MOGF	76.37252	308.53359	39.9620	-120.6502	39.5362	-119.9492
GZY	MOGN	80.07540	305.32496	39.9620	-120.6502	39.5481	-119.8836

GZY	MOGW	77.68072	308.41313	39.9620	-120.6502	39.5301	-119.9360
GZY	NMHS	88.8	302	39.9620	-120.6502	39.5309	-119.7754
NOAA	GZY	85.15120	120.68017	39.5681	-119.7958	39.9620	-120.6502
PICO	GZY	95.29942	127.98521	39.4312	-119.7756	39.9620	-120.6502
RFNV	GZY	82.48023	121.25543	39.5742	-119.8275	39.9620	-120.6502
SKYF	GZY	87.83447	127.11127	39.4825	-119.8340	39.9620	-120.6502
BAB	*CF01*	*57.1*	*149*	*39.6013*	*-120.1040*	*39.1593*	*-119.7647*
BAB	*CF02*	*55.2*	*145*	*39.6013*	*-120.1040*	*39.1907*	*-119.7418*
BAB	*CF03*	*60.3*	*151*	*39.6013*	*-120.1040*	*39.1257*	*-119.7676*
BAB	*GSCB*	*41.7*	*177*	*39.6013*	*-120.1040*	*39.2267*	*-120.0812*
DIX	MOGB	159.81050	79.00490	39.8022	-118.0820	39.5425	-119.9186
DIX	MOGC	161.47614	78.54654	39.8022	-118.0820	39.5285	-119.9348
DIX	MOGF	162.51997	78.91960	39.8022	-118.0820	39.5362	-119.9492
DIX	MOGN	156.74591	79.04161	39.8022	-118.0820	39.5481	-119.8836
HONJ	DIX	161.04101	259.78669	39.5307	-119.9302	39.8022	-118.0820
MOGA	DIX	162.50707	259.55085	39.5222	-119.9454	39.8022	-118.0820
MOGE	DIX	160.51	260.55495	39.5217	-119.9216	39.8022	-118.0820
MOGW	DIX	161.54180	259.79835	39.5301	-119.9360	39.8022	-118.0820
DON	MOGB	40.50773	238.54517	39.3517	-120.3205	39.5425	-119.9186
DON	MOGC	38.51503	239.43164	39.3517	-120.3205	39.5285	-119.9348
DON	MOGF	37.91187	237.35875	39.3517	-120.3205	39.5362	-119.9492
DON	MOGN	43.40513	239.93278	39.3517	-120.3205	39.5481	-119.8836
HONJ	DON	38.97911	59.17190	39.5307	-119.9302	39.3517	-120.3205
MOGA	DON	37.37627	59.40235	39.5222	-119.9454	39.3517	-120.3205
MOGE	DON	39.12	56.87694	39.5217	-119.9216	39.3517	-120.3205
MOGW	DON	38.51745	58.88089	39.5301	-119.9360	39.3517	-120.3205
EBP	MOGB	107.14856	174.77304	38.5828	-119.8063	39.5425	-119.9186
EBP	MOGC	105.73607	173.93622	38.5828	-119.8063	39.5285	-119.9348
EBP	MOGF	106.72404	173.31644	38.5828	-119.8063	39.5362	-119.9492
EBP	MOGN	107.53895	176.41780	38.5828	-119.8063	39.5481	-119.8836
HONJ	EBP	105.93848	354.24334	39.5307	-119.9302	38.5828	-119.8063
MOGA	EBP	105.14013	353.48417	39.5222	-119.9454	38.5828	-119.8063
MOGE	EBP	104.86	354.75752	39.5217	-119.9216	38.5828	-119.8063
MOGW	EBP	105.92388	353.97200	39.5301	-119.9360	38.5828	-119.8063
NMHS	EBP	105.45299	1.44001	39.5309	-119.7754	38.5828	-119.8063
NOAA	EBP	109.55926	0.47069	39.5681	-119.7958	38.5828	-119.8063
PICO	EBP	94.37088	1.60102	39.4312	-119.7756	38.5828	-119.8063
RENO	EBP	106.33297	359.65345	39.5391	-119.8138	38.5828	-119.8063
RFNV	EBP	110.24895	359.05565	39.5742	-119.8275	38.5828	-119.8063
SKYF	EBP	100.06625	358.63870	39.4825	-119.8340	38.5828	-119.8063

SMRN	EBP	106.33813	3.64807	39.5372	-119.7274	38.5828	-119.8063
SPHI	EBP	106.91507	2.25222	39.5436	-119.7573	38.5828	-119.8063
SWTP	EBP	104.18581	4.85529	39.5164	-119.7035	38.5828	-119.8063
UNRN	EBP	104.99046	359.45237	39.527	-119.818	38.5828	-119.8063
UNRX	EBP	103.66815	2.70344	39.5141	-119.7493	38.5828	-119.8063
CF01	EMB	35.61239	54.72061	39.1593	-119.7647	38.9748	-120.1019
CF02	EMB	39.27154	52.20452	39.1907	-119.7418	38.9748	-120.1019
GSCB	EMB	28.06566	3.64236	39.2267	-120.0812	38.9748	-120.1019
HVGC	EMB	65.98870	29.69915	39.4897	-119.7209	38.9748	-120.1019
HONJ	EMB	63.55384	13.39683	39.5307	-119.9302	38.9748	-120.1019
MOGA	EMB	62.33929	12.43452	39.5222	-119.9454	38.9748	-120.1019
MOGE	EMB	62.76	13.54581	39.5217	-119.9216	38.9748	-120.1019
MOGW	EMB	63.37455	12.97364	39.5301	-119.9360	38.9748	-120.1019
EMB	MOGB	65.06530	194.09466	38.9748	-120.1019	39.5425	-119.9186
EMB	MOGC	63.22470	193.20670	38.9748	-120.1019	39.5285	-119.9348
EMB	MOGF	63.79152	191.94201	38.9748	-120.1019	39.5362	-119.9492
EMB	MOGN	66.45784	196.49592	38.9748	-120.1019	39.5481	-119.8836
NMHS	EMB	67.92318	24.34560	39.5309	-119.7754	38.9748	-120.1019
NOAA	EMB	71.03620	21.67544	39.5681	-119.7958	38.9748	-120.1019
PICO	EMB	58.01463	28.88423	39.4312	-119.7756	38.9748	-120.1019
RENO	EMB	67.46935	21.47896	39.5391	-119.8138	38.9748	-120.1019
RFNV	EMB	70.70853	19.42689	39.5742	-119.8275	38.9748	-120.1019
SKYF	EMB	60.98487	22.14773	39.4825	-119.8340	38.9748	-120.1019
SMRN	EMB	70.35639	27.15827	39.5372	-119.7274	38.9748	-120.1019
SPHI	EMB	69.85749	25.02211	39.5436	-119.7573	38.9748	-120.1019
SWTP	EMB	69.30657	29.54336	39.5164	-119.7035	38.9748	-120.1019
UNRN	EMB	66.08620	21.61927	39.527	-119.818	38.9748	-120.1019
UNRX	EMB	67.21353	26.74382	39.5141	-119.7493	38.9748	-120.1019
IND	HONJ	32.82286	251.05474	39.4343	-120.2917	39.5307	-119.9302
IND	MOGA	31.28652	251.90682	39.4343	-120.2917	39.5222	-119.9454
IND	MOGB	34.20194	249.52393	39.4343	-120.2917	39.5425	-119.9186
IND	MOGC	32.37048	251.23461	39.4343	-120.2917	39.5285	-119.9348
IND	MOGE	33.2	247.77244	39.4343	-120.2917	39.5217	-119.9216
IND	MOGF	31.49991	249.02770	39.4343	-120.2917	39.5362	-119.9492
IND	MOGN	37.23409	250.26309	39.4343	-120.2917	39.5481	-119.8836
IND	MOGW	32.33090	250.87666	39.4343	-120.2917	39.5301	-119.9360
MPK	HONJ	27.50551	198.23059	39.2957	-120.0302	39.5307	-119.9302
MPK	MOGA	26.21704	196.16044	39.2957	-120.0302	39.5222	-119.9454
MPK	MOGB	29.06783	199.29104	39.2957	-120.0302	39.5425	-119.9186
MPK	MOGC	27.15140	197.59843	39.2957	-120.0302	39.5285	-119.9348

MPK	MOGE	26.8	198.17830	39.2957	-120.0302	39.5517	-119.9216
MPK	MOGF	27.63158	194.61046	39.2957	-120.0302	39.5362	-119.9492
MPK	MOGN	30.75979	204.21146	39.2957	-120.0302	39.5481	-119.8836
MPK	MOGW	27.29029	197.27878	39.2957	-120.0302	39.5301	-119.9360
P07A	CF01	86.34924	60.37671	39.5399	-118.8893	39.1593	-119.7647
P07A	CF02	82.93341	61.81426	39.5399	-118.8893	39.1907	-119.7418
P07A	CF03	88.46854	58.35135	39.5399	-118.8893	39.1257	-119.7676
P07A	NMHS	75.99221	88.96346	39.5399	-118.8893	39.5309	-119.7754
P07A	NOAA	77.77736	92.02179	39.5399	-118.8893	39.5681	-119.7958
P07A	PICO	77.01163	80.68898	39.5399	-118.8893	39.4312	-119.7756
P07A	RENO	79.27387	89.64143	39.5399	-118.8893	39.5391	-119.8138
P07A	RF05	81.26504	87.31494	39.5399	-118.8893	39.5095	-119.8360
P07A	RFNV	80.51858	92.41605	39.5399	-118.8893	39.5742	-119.8275
P07A	SMRN	71.86688	89.49389	39.5399	-118.8893	39.5372	-119.7274
P07A	SPHI	74.42784	90.04039	39.5399	-118.8893	39.5436	-119.7573
P07A	SWTP	69.87620	87.59791	39.5399	-118.8893	39.5164	-119.7035
PAH	HONJ	50.68585	67.14178	39.7065	-119.3842	39.5307	-119.9302
PAH	MOGA	52.25552	66.73260	39.7065	-119.3842	39.5222	-119.9454
PAH	MOGB	49.26650	68.10597	39.7065	-119.3842	39.5425	-119.9186
PAH	MOGC	51.14444	67.05803	39.7065	-119.3842	39.5285	-119.9348
PAH	MOGE	50.4	159.37775	39.7065	-119.3842	39.5217	-119.9216
TAH	MOGB	48.43820	205.78988	39.1500	-120.1630	39.5425	-119.9186
TAH	MOGC	46.43578	205.07163	39.1500	-120.1630	39.5285	-119.9348
TAH	MOGF	46.71160	203.24522	39.1500	-120.1630	39.5362	-119.9492
TAH	MOGN	50.36363	208.57852	39.1500	-120.1630	39.5481	-119.8836
TAH	MOGA	45.41913	204.40048	39.1500	-120.1630	39.5222	-119.9454
TAH	MOGE	46.25	205.00082	39.1500	-120.1630	39.5217	-119.9216
TAH	MOGW	46.55362	204.86336	39.1500	-120.1630	39.5301	-119.9360
TAH	HONJ	46.82521	205.38494	39.1500	-120.1630	39.5307	-119.9302
YER	EGLV	45.62002	114.86498	38.9845	-119.2407	39.1580	-119.7196
YER	NMHS	76.22502	142.67830	38.9845	-119.2407	39.5309	-119.7754
YER	NOAA	80.58239	143.45978	38.9845	-119.2407	39.5681	-119.7958
YER	PICO	67.75518	136.97389	38.9845	-119.2407	39.4312	-119.7756
YER	RENO	78.97402	141.15537	38.9845	-119.2407	39.5391	-119.8138
YER	RF05	77.68635	138.52415	38.9845	-119.2407	39.5095	-119.8360
YER	RFNV	82.76441	142.20819	38.9845	-119.2407	39.5742	-119.8275
YER	SKYF	75.34632	137.11115	38.9845	-119.2407	39.4825	-119.8340
YER	SMRN	74.37946	145.55902	38.9845	-119.2407	39.5372	-119.7274
YER	SWTP	71.31393	145.88182	38.9845	-119.2407	39.5164	-119.7035
YER	UNRN	78.16018	140.32847	38.9845	-119.2407	39.527	-119.818

YER	CCAD	50.54808	113.11394	38.9845	-119.2407	39.1642	-119.7786
YER	CF01	49.23205	113.08714	38.9845	-119.2407	39.1593	-119.7647
YER	CF02	48.94836	117.77224	38.9845	-119.2407	39.1907	-119.7418
YER	CF03	48.12715	108.87333	38.9845	-119.2407	39.1257	-119.7676
YER	EGLV	45.62002	114.86498	38.9845	-119.2407	39.1580	-119.7196
NMHS	WVA	46.17554	174.82130	39.5309	-119.7754	39.9445	-119.8240
NOAA	WVA	41.92128	176.69458	39.5681	-119.7958	39.9445	-119.8240
PICO	WVA	57.22388	175.83437	39.4312	-119.7756	39.9445	-119.8240
RFNV	WVA	41.17474	180.41742	39.5742	-119.8275	39.9445	-119.8240
SKYF	WVA	51.37690	180.95711	39.4825	-119.8340	39.9445	-119.8240
SMRN	WVA	46.03464	169.63356	39.5372	-119.7274	39.9445	-119.8240
SPHI	WVA	44.93934	172.68855	39.5436	-119.7573	39.9445	-119.8240
SWTP	WVA	48.70294	167.74698	39.5164	-119.7035	39.9445	-119.8240
UNRN	WVA	46.42466	179.36490	39.527	-119.818	39.9445	-119.8240
WVA	RENO	45.08486	358.89492	39.9445	-119.8240	39.5391	-119.8138
WVA	UNRX	48.28061	352.42096	39.9445	-119.8240	39.5141	-119.7493

Part 2.

A higher resolution seismic velocity model in the Reno Basin estimated from ambient - seismic noise.

I. M. Tibuleac
Nevada Seismological Laboratory, U. Nevada, Reno NV 89557
ileana@seismo.unr.edu

INTRODUCTION

Our primary goal was to provide improved resolution and shallow (< 5 km deep) constraints to the existing 3-D velocity models of the Reno Basin using previously unexploited ambient noise information from recordings at instruments deployed in 2008, during a large earthquake sequence in West Reno, as well as from recordings at permanent ANSS and Nevada Network stations. The temporary deployments, including accelerometers, broadband sensors and high frequency geophones with "Texan" digitizers, were prompted by an unusually shallow swarm of earthquakes in west Reno in 2008 (Anderson *et al*., 2008). This sequence (Anderson *et al*., 2009), with a main shock at 06:40 UTC on April 26, 2008, M_L=4.7, M_W=5.0, and a hypocentral depth of 3.1 km, "illuminated" the Reno Basin for at least six months in 2008. The strongest peak vector acceleration was 1164 cm/s^2, or about 1.19 g, at the station MOGL, located in a residence ~0.4 km from the epicenter, at a frequency of about 3 Hz. The mean horizontal peak velocity exceeded 12 cm/s at all four local stations, and the peak vector velocity at the strongest was 54 cm/s.

The Reno Basin, a geomorphic flat region of Quarternary deposits (Pancha *et al*., 2007) is a fault-controlled basin 13-km wide and 21-km long. The basin area has been delineated by gravity studies (Abbott and Louie, 2000) and includes the Reno–Sparks urban area. Shallow seismic velocity (depth less than 100 m) has been estimated by Pancha *et al*., 2007 and Scott *et al*., 2008 while deeper (3-10 km) P/S velocity models have been estimated by Preston and von Seggern, 2008. To improve the resolution of the Community Velocity Model (CVM) in the area (Louie *et al*., 2010) a study by Tibuleac *et al*., 2011 (Part 1 of this report) used ambient seismic noise to estimate shear velocity models deeper than 1.5 km in the Reno Basin.

In this study, we estimated P/S velocity models in the upper five km of the crust in the Reno Basin, using a first prototype of a transportable and cost-effective method based on ambient seismic noise and seismic signal processing. We also used station pairs including broadband sensors, accelerometers and high frequency geophones for the first time at a small-basin scale (hundreds of meters to tens of km). The model constraints derived from this study provided essential new information for the CVM, which needed improved resolution for realistic estimates of the ground motion (Louie *et al*., 2010). We used ambient seismic noise interferometry to extract Green's Functions from crosscorrelation of continuous records at the Reno Basin stations. Surface waves and compressional wave reflections were identified between pairs of stations. We also used autocorrelations at all the Reno Basin stations to distinguish reflecting layers beneath each station.

Seismic interferometry is a relatively new technique (Campillo and Paul, 2003; Lobkis and Weaver, 2001; Larosse *et al*., 2005; Weaver and Lobkis, 2004). Seismic noise

can be processed at all frequencies, starting with the high range (tens of Hz) down to 30-40 second period Rayleigh or Love waves, for inter-station distance respectively from meters to hundreds of km. The technique is based on the theoretical result which states that if A and B are two passive sensors (seismic stations), the Green's Function, or the signal that B would receive when A is given an impulsive excitation, can be recovered from the temporal cross-correlation of incoherent ambient noise received at A and B.

Over the past decade, ambient seismic noise tomography has provided important constraints on 3D crustal structure in many regions in the world, including the western United States (Sabra *et al*., 2005; Shapiro *et al*., 2005; Lin *et al*., 2008; Bensen *et al*., 2008; Lin *et al*., 2008, Yang and Ritzwoller, 2008). The lateral extent of most of these studies ranged from several hundred to several thousand kilometers, with inter-station distances more than 60 kilometers and period range 5 to 30 sec, thus sampling deeper than 5 km. A study of an area in the Taipei Basin, China, with similar dimensions to the Reno Basin has been published by Huang *et al*., 2010. We used algorithms for extracting ambient noise-derived Green's functions (Lin *et al*., 2008, Yang *et al*., 2008) developed at the Nevada Seismological Laboratory (NSL) (Tibuleac *et al*., 2011, von Seggern *et al*, 2009) to derive velocity models in the Reno Basin, for inter-station distance less 60 km, and for different sensor types. The algorithms were closely following the Bensen *et al*., 2007 method. We have included, however, modifications to account for different-instrument pairs and smaller inter-station distance analysis. Modifications included distance-dependent filtering and data processing after conversion into records of the same instrument type, i.e. broadband with 0.1 Hz corner frequency.

In a high hazard region such as Reno-Carson city, with potential for large magnitude (M7-7.5) events (dePolo *et al*., 1997), the results of our proposed study had the potential to improve understanding of the 3-D structure, including basin geometries. Improved velocity models would result in realistic ground shaking estimates and would aid in first-response planning. By improving our understanding of expected ground motions, the results of the proposed research had the potential to reduce losses from earthquakes in the Reno community. Our study built on an NSL on-going effort to assemble a Reno Basin Community Velocity Model (CVM) through integration and validation of new and existing data sets (Louie et al., 2010).

In this study, we addressed limitations of the previous work as follows: First, we added supplementary information to CVM seismic velocity models by examination of P and S components of the Green's Functions extracted from ambient noise and signal crosscorrelation stacks. We analyzed Rayleigh wave periods from 0.2 to 8 sec, providing shear velocity models for the upper 8 km of the Reno Basin. Second; the 2008 earthquake swarm source area in west Reno had unidirectional arrivals and the lack of reversed profiles was a limitation of a tomography study using the "Texan" deployment. In contrast, hundreds of inter-station paths have been analyzed in our study, yielding higher resolution in the upper crust of the Reno Basin. Third, the previous shear velocity model estimates used only permanent station records from 2006-2008. In this project we used temporary stations deployed in 2008 (Figure 1), leading to an unprecedented station coverage in the area. Last, very shallow (less than 200 m from the surface) velocity profiles were derived for ANSS station sites (Pancha *et al*., 2007). However, little was known about deeper structure, to 3 km depth. We estimated reflector depth in the upper

two km by use of continuous waveform autocorrelation beams at each station in the Reno Basin.

In summary, to investigate crustal structure in the upper eight km, we measured fundamental mode Rayleigh group velocity from Green's Functions extracted from all available station pairs in the Reno Basin and vicinity. Autocorrelation beams were estimated at all available stations for a time length from three days to two years to obtain independent constraints on the velocity model. Where possible, the GF *P*-component velocity was measured. We estimated fundamental Rayleigh phase group velocity maps and then inverted the model in each grid cell for crustal structure. The new model was integrated with an updated CVM, using newly developed Matlab algorithms. Finally, we discussed the geologic implications of the new models and the integration of the new information into the CVM.

DATABASE

We processed ambient noise in the Reno and Carson City basins, in an area of 60 x 60 km^2 to derive new crustal *P* and *S* seismic velocity models. To estimate an accurate initial *S*-velocity model, we analyzed Green's Functions extracted for pairs of stations within 30 km from UNRN (39.527N, 119.818W). UNRN is an ANSS station located approximately in the center of the Reno Basin.

The database included waveforms recorded in 2008 at temporary seismic stations (Figure 1) deployed in the Reno Basin in 2008 by the Nevada Seismological Laboratory (NSL), with support from Institutions for Research in Seismology (IRIS), records of a network of twenty one ANSS stations, three permanent broadband and six permanent short period stations (Table 1). The temporary seismic stations were the Mogul RAMP deployment and the "Texan" deployment.

The Mogul RAMP deployment: As an earthquake swarm in Mogul, NV, escalated from February 2008, with a peak on April 26 2008, NSL installed an array of portable stations (Anderson *et al*., 2008) in west Reno. The array included initially four (within 1 km), and ultimately, nine (within 10 km) IRIS RAMP broadband, three-component stations (Figure 1, lower right inset). These six-component stations included broadband Trillium sensors and force-balance accelerometers (Episensors). The stations recorded continuous waveforms for approximately two months.

The “Texan” deployment: As described by Dhar *et al*., 2008, from May 15 to July 15, 2008 NSL deployed ninety Flexible Array single-channel RefTek RT-125A IRIS recorders equipped with continuously recording vertical 4.5-Hz, high frequency geophones. The sensors were deployed in Reno and Sparks in five consecutive four-day deployments (at a total of 103 locations). The Julian days corresponding to the five deployments in 2008 were 140 to 144, 150 to 153, 169 to 175, 176 to 182 and 183 to 189. We expected the high frequency geophones to be useful for analysis of *Rg* with frequencies of 0.5 Hz and higher, as demonstrated by Leidig *et al*., 2006. The highest frequency *Rg* extracted by Leidig *et al*., 2006 from explosions at distances from 1-15 km from raw seismograms was 4 Hz. Although we did not use explosions, the high seismic activity in Mogul at the time of the experiment illuminated the basin with significant amounts of low-frequency energy during the study period.

METHOD

The analysis method includes the following steps:

1. Estimate an initial P/S velocity model, using an updated version of the existing NSL Reno Basin model. CVM models mentioned above were integrated with newly derived models for the study area, using a new set of Matlab algorithms named MAT_MOD. In MAT_MOD, a series of depths of interest were chosen for all models. Each model was stored into a Matlab structure. The structure includes the reference to the model; the model area (which is a square oriented North-South, East-West; and the model. The model consists of eleven columns: depth, P velocity in km/s, S velocity in km/s, density (g/cm^3), P and S attenuation factors Q_p and Q_s and five trust factors, one for *P,S,*density, Q_p and Q_s. For a "no information" point, the parameter value is set to -99. The "trust" factor ranges from 0 to 1 and is, for example, set by the analyst up to 0.9 for reflection/refraction lines and is set to 0.01 for general (non-local) models. Using the "trust" parameter, seismic lines and local data are given higher weights than the global model weights. A "slack" factor (in this case 0.04˚) for each model represents a chosen extension of the model area. When, for example, the P/S-velocity model at a point characterized by latitude and longitude is requested by the user, the program finds all the models including a square centered on the respective point. A side of the square is twice the slack value. For example, the resulting *P*-velocity at the respective point is a "trust" - parameter weighted mean, after the "-99" estimates are discarded.

2. Refine the initial model using P-velocity estimates from ambient noise crosscorrelations and autocorrelations. Not only the surface wave portion of the Green's function can be retrieved from inter-station ambient noise cross-correlation, the body wave component has also been previously extracted.

2.1. The P-wave component of the ambient-noise crosscorrelation - derived Green's Function has been seldom identified (Tibuleac et al., 2011, Ryberg, 2011) because of low *P*-arrival SNR. It was also difficult to identify weak arrivals without array analysis. Also, according to Ruigrok et al., 2011, P-waves are more likely obtained for paths with enhanced seismic energy in the respective frequency band. In this study we used arrival time and record sections to identify *P*-arrivals.

2.2. We used continuous waveform auto-correlation to extract the GF reflection component at each station. Claerbout (1968) showed that for a horizontally layered medium the auto-correlation of the transmission response of a seismic noise source in the subsurface yields the reflection response. New studies (Sanchez-Sesma et al., 2012) theoretically demonstrated that functional forms of both the imaginary part of Green's function (in frequency) and the reflection seismograms are remarkably similar. Body-wave reflections (primaries as well as multiples) from layer interfaces were retrieved by Draganov *et al*., 2007. Automatic gain control (AGC) has been applied like in Tibuleac and von Seggern, 2012.

4. Extract the GF surface wave component, and estimate group and phase velocity dispersion curves. The largest amplitude GF component in our study area is the fundamental Rayleigh wave. The "rule of thumb" is that the inter-station distance should be at least two-three times to several tens of times larger than the maximum wavelength of the seismic phases of interest. Another rule-of-thumb is that the depth best probed by fundamental Rayleigh waves is usually ~1/3 of the Rayleigh seismic wavelength. Thus,

GF extraction is conditional on the inter-station distance. After waveform conversion to broadband sensor velocity, combinations of all the available stations were investigated. We analyzed waveforms recorded at more than 10000 station pairs at distance from 0.2 km to 60 km (Figure 2). Continuous records were crosscorrelated and beamed. Only the highest signal-to-noise ratio GF's were used. The variation in elevation across the study region was less than 300 m, except for stations PEA, BAB and VPK, which were at over 600-1000 m elevation difference from the rest of the stations in the study area. The associated bias at lower than 300 m elevation difference was less than 1% (see also Huang *et al*., 2010). The bias at 600-1000 m elevation difference was also much smaller than the inferred variations in group velocity (~ 0.5 km/s), thus, we ignored the effects of topography in this study. We recognize, however, the necessity of further investigations, to better quantify the elevation effects.

4. Invert for new, higher resolution seismic velocity models and integrate the new models into CVM. Once the GF's were visually inspected we used CPS3.3 algorithm *do_mft* (Herrmann and Ammon, 2002) to estimate fundamental mode Rayleigh dispersion curves. We inverted all the available group velocity measurements in the study region (including the measurements reported by Louie et al., 2010) to derive shear-velocity models.

To estimate a group velocity tomographic model and to perform grid-dispersion inversion we used the code gridsp, written by Dr. Hafidh Ghalib. *gridsp* allowed the use of sources and origins only within the region of interest (32˚ N to 45.6˚ N and 123.6˚ W to 110˚ W). The propagations paths were assumed to be straight rays. A stochastic inversion method (Dr. Hafidh Ghalib, personal communication) was used (Feng and Teng, 1983). Given the dispersion curves of surface waves over varying tectonic units, the pure-path dispersion curves were determined for each grid block or element. The models were added to the CVM using the same procedure as at Step 1.

RESULTS

1. Estimate an initial P/S velocity model, to be used in inversions, using an updated version of the existing NSL Reno Basin model. Examples of the initial velocity model at zero km depth (~ 1.4 km beneath the surface) and at 1.5 km depth (~ 3 km below the surface) in the Reno basin are shown in Figure 3. The starting model includes the existing CVM to which ambient noise - extracted shear wave velocity was added.

The starting model has been assembled from a *3-D P*- and *S*-wave velocity model 3-20 km from the surface (Preston and von Seggern, 2008); vs30 and vs100 measurements 30-200 m from the surface (Pancha *et al*. 2004; Scott *et al*. 2004, Louie *et al*. 2006) and structural estimates from gravity in the basins ~ 30 m from the surface (Abbott and Louie, 2000). Validation of this Community Velocity Model (CVM) by Louie *et al*., 2009, with a finite-difference 3-D elastic waveform calculation code, showed the need a higher CVM resolution to produce more realistic waveforms. To these models we have added a new shear velocity model derived from ambient noise analysis during a previous NHRP study (Louie *et al.*, 2010). Velocity models estimated by Tibuleac *et al*., 2011) (Chapter 1 in this report) from ambient seismic noise using array processing were also added to this model. Tibuleac *et al*., 2011 analyzed ambient noise crosscorrelation-derived Green's functions which sampled the upper 2-10 km of the crust

(surface wave periods from 2-10 sec) using cross-correlation between waveforms recorded at permanent seismic stations (including ANSS accelerometers) within the Reno and Carson City area basins (von Seggern *et al*. 2009) and temporary broadband stations deployed in Mogul, NV. A total of 150 models were used for the initial integrated model (Figure 3).

2. *Refine the initial model using P-velocity estimates from ambient noise crosscorrelations and autocorrelations.*

2.1. A strong source of seismic signals has been illuminating the basin from Mogul, west Reno, NV in 2008, which may explain *P*-arrival information extraction in Figures 4 and 6. In these figures *P*-velocity has been estimated by an analyst. Estimated P-velocity for station pairs not including geophones is shown in Figure 5. When added to the CVM, in each model the *P*-velocity was attributed to a layer with maxim depth equal to half of the inter-station distance. Table 2 shows the station pairs used in Figures 6 and 9.

3.2. We calculated autocorrelations at all the Reno Basin stations to extract the *P*-reflection component of the GF's and to estimate the depth of reflecting layers beneath each station. Results for two lines (Table 3) were selected for analysis (Figure 7): Line 1 crossing the Reno Basin to the north and Line 2, south of Hwy 80. Line 2 is along a profile characterized by Abbott and Louie, 2000 and Scott et al., 2006. The results did show differences, attributed to basin structure. On Line 1, below the Mogul array the profile shows a clear first reflector at 1 s (two-way travel time), a second reflector at ~2 s is observed to the east. The 2 s reflector is visible on the profile south of Truckee River. Our main observation is that deeper reflection layers are observed when filtering the GF reflection component in lower frequency bands. In Figure 7 the waveforms were filtered from 4-8 Hz.

4. *Extract the GF surface wave component, and estimate group velocity dispersion curves.* Continuous records at the Reno Basin temporary and permanent stations were crosscorrelated and beamed. Signal to noise ratio was estimated as the decimal logarithm of the ratio of the maxim amplitude of the signal and twice the standard deviation of the noise (Tibuleac and Britton, 2005) for *P* and *Rg* arrivals. Based on empirical observations, the *Rg* signal window was chosen from 0.4 km/s to 1 km/s for inter-station distance less than 1km, from 0.8 km/s to 2 km/s for inter-station distance from 1 to 5 km, from 1 km/s to 2.5 km/s for inter-station distance from 5 to 10 km and from 1.5 km/s to 3.5 km/s for inter-station distance from 10 to 15 km. *P*-velocity windows were chosen the start to the start of the *Rg*-search window. In each case, an equal length noise window was chosen to end 5 sec before the last GF time series sample point. SNR was estimated in several empirically determined frequency ranges: 0.5 - 1 Hz, 1-2 Hz and 2-4 Hz. Although more than 10,000 station pairs (including geophones) were investigated, only 230 station pairs were selected for analysis. Algorithms for SNR calculation were applied to sort station pairs including geophones, choosing SNR>1.1. Visual analysis was the basis for the selection of station pairs including broadband, accelerometer and short-period sensors. Examples of GF fundamental Rayleigh component were shown in Figures 8 and 9.

4. Invert for new, higher resolution seismic velocity models.

Plots of the fundamental mode Rayleigh group velocity dispersion curves extracted in the study area were shown in Figure 10. The mean dispersion curve

estimated in the study area (Table 4) using interpolated Rayleigh group velocity from 230 inter-station pairs was compared to a dispersion curve estimated from the Priestley and Brune, 1980 surface wave velocity model in Nevada (which, however, does not contain information at periods less than 5 s).

For tomographic inversion, the study region (39.2 N, 120.3 W to 39.88 N, 119.62 W) was divided into 16x16 km constant group velocity cells (0.04 degrees on one side). Figure 12 shows the number of paths per grid unit. The period range of the dispersion curves was from 0.5 s to 18 s.

Examples of fundamental Rayleigh group velocity maps estimated at three periods considered significant are shown in Figure 13. The velocity at each grid point was inverted for shear velocity models using the *surf96* algorithms of the CPS3.3 waveform analysis package. The starting model for surface wave velocity model inversion was estimated from a model inspired by Priestley and Brune, 1980 and was the same at each grid node (Table 5). Pending CVM validation, the starting model should be the model extracted from the CVM instead. The resulting shear velocity models at depths from 0.5 to 5.5 km from the surface are shown in Figure 14. The maxim standard error of the surf96 dispersion fit of the estimated and observed models was ~ 0.3 km/s for all the grid points. The velocity model at each grid point was integrated into the CVM model using newly developed Matlab codes.

DISCUSSION AND CONCLUSIONS

We have developed a non-invasive, inexpensive method for processing information extracted from ambient seismic noise on inter-sensor paths in an area of 60 km^2. The GF *P* and *S*- arrival components have been extracted in the Reno Basin and vicinity on paths between broadband, short period, and high frequency sensors. Considering that the GF's were extracted using early versions of our codes, which did not yet have options for choosing the highest SNR daily GF's when forming the crosscorrelation beams, we considered the results encouraging. Using phase-specific, *SNR*-based sorting algorithms, we have extracted the fundamental mode Rayleigh wave component of the GF's with the highest SNR. The information was used to estimate group velocity maps of the study area. *P*-phase information has been independently added to the CVM, using the MAT_MOD set of algorithms.

There was a good correlation between the surface wave group velocity maps (Figure 13), the shear wave models (Figure 14) and the geological features of the Reno Basin (Pancha *et al.*, 2007). Slow velocity regions (Figure 13, 14) corresponded to sedimentary basins. Faster velocities characterized the Sierra Nevada mountain range. As expected for the inter-station range available in this study, shear velocity models at depths 0.5 - 8 km from the surface were resolved.

The newly developed method has greatly benefitted from the existence of a broadband array. Array record sections made possible identification of GF phase components, which is a non-trivial exercise at short distances and at low phase SNR. Station pairs including one geophone were observed to be more effective in GF extraction when the second station was a broadband or short period sensor, or an accelerometer than when the second station was another geophone. Pending model

validation using earthquake and explosion data, our contribution to CVM through estimation of P/S models should be considered as preliminary and non-unique,

REFERENCES

Abbott, R. E., and J. N. Louie, 2000, Depth to bedrock using gravimetry in the Reno and Carson City, Nevada area basins, *Geophysics*, 65, 340-350.

Anderson, J. G., I. Tibuleac, R. Anooshehpoor, G. Biasi, D. von Seggern and K. Smith 2009. Exceptional Ground Motions Recorded During the 26 April, 2008, MW=5.0 Earthquake in Mogul, Nevada, Bull. Seism. Soc. Am., 99, No. 6, 3475–3486, doi: 10.1785/0120080352

Anderson, J. G., I. Tibuleac, R. Anooshehpoor, G. Biasi and K. Smith (2008), Ground Motions Recorded During the 26 April, 2008, MW=5.0 Earthquake in Mogul, Nevada, Eos Trans. AGU, 89(53), Fall Meet. Suppl., Abstract S53C-04.

Bensen, G. D., M. H. Ritzwoller, and N. M. Shapiro (2008). Broadband ambient noise surface wave tomography across the United States, J. Geophys. Res. 113, B05306, doi 10.1029/2007JB005248.

Bensen, G.D., M.H. Ritzwoller, M.P. Barmin, A.L. Levshin, F. Lin, M.P. Moschetti, N.M. Shapiro, and Y. Yang. Processing seismic ambient noise data to obtain reliable broad-band surface wave dispersion measurements, *Geophys. J. Int.* **169**, 1239-1260 (2007)

Campillo, M. and A. Paul, 2003. Long-Range correlations in the diffuse seismic coda, *Science*, 229, 547-549.

Claerbout J. F., 1968. Synthesis of a layered medium from its acoustic transmission response, Geophysics, 33, 264-269.

Clark, M., Louie, J., Pancha, A., Scott, J., and Heath, K., 2005, Geophysical investigation of a fault as a hydrologic barrier in Reno, Nevada, presented at the *Seismol. Soc. of Amer. Ann. Mtg., Lake Tahoe, Nevada*, April 26-29.

Cho, K. H., R. B. Herrmann, C. J. Ammon, and K. Lee, 2007. Imaging the Upper Crust of the Korean Peninsula by Surface-Wave Tomography, *Bull. Seism. Soc. Am.*, **97**, No. 1B, 198–207, doi: 10.1785/0120060096.

dePolo, C. M., J. G. Anderson, D. M. dePolo, J. G. Price, 1997, Earthquake occurrence in the Reno–Carson City urban corridor: *Seismol. Res. Lett.*, 68, 401-412.

Dhar, M, S., Thompson M., Kell-Hills A., Louie J. N., Smith K. D., Tirabassi J., Tom S. and Irwin T (2008), Educating a Community Impacted by an Earthquake Swarm: 106 Volunteers Host Earthscope Flexible Array Recorders During the Mogul, Nevada sequence, Eos Trans. AGU, 89(53), Fall Meet. Suppl., Abstract PA13B-1342 1340h

Draganov, D., K. Wapenaar, W. Mulder, J. Singer, and A. Verdel. Retrieval of reflections from seismic background-noise measurements. *Geophys. Res. Letts.* **34**, L04305, doi: 10.1029/2006GL028735 (2007).

Feng, C. C. an T. L. Teng (1983). Three-dimensional crust and upper mantle structure of the Eurasian continent, J. Geophys. Res., 88, 2261-2272.

Frary, R.N., Stephenson, W.J., Louie, J.N., Odum, J.K., Maharrey, J.Z., Messmer, M.L., Tomlinson, I., Littlefield, E.F., Hughes, A., Jha, S., Kohls, K., Dhar, M.S., Konkol, S., Wakwak, A., Cashman, P.H., Trexler, J.H., Kent, R., Hoffpauir, C.,

2009. Preliminary analysis of high-resolution seismic imaging profiles acquired through Reno, Nevada, for earthquake hazard assessment, Abstract.

Frank, S. D., A. E. Foster, A. N. Ferris, and M. Johnson, 2009. Frequency-Dependent Asymmetry of Seismic Cross-Correlation Functions Associated with Noise Directionality, *Bull. Seism. Soc. Am.*, **99**: 462-470

Herrmann, R.B., Ammon, C.J., 2002. Computer Programs in Seismology – SurfaceWaves, Receiver Functions and Crustal Structure. Saint Louis University, http://www.eas.slu.edu/People/RBHerrmann/ComputerPrograms.html.

Huang, Yu-Chih, Huajian Yao, Bor-Shouh Huang, Robert D. van der Hilst, Kuo-Liang Wen, Win-Gee Huang, and Chi-Hsuan Chen, 2010. Phase Velocity Variation at Periods of 0.5–3 Seconds in the Taipei Basin of Taiwan from Correlation of Ambient Seismic Noise, *Bulletin of the Seismological Society of America*, Vol. 100, No. 5A, pp. 2250–2263, October 2010, doi: 10.1785/0120090319

Gouedard P., L. Stehly1, F. Brenguier, M. Campillo, Y. Colin de Verdiere, E. Larose1, L. Margerin, P. Roux, F. J. Sanchez-Sesma, N. M. Shapiro and R. L. Weaver, 2008. Cross-correlation of random fields: mathematical approach and applications, *Geophysical Prospecting*, 2008, **56**, 375–393.

Groos, J. C. and J.R.R. Ritter, 2009. Time domain classification and quantification of seismic noise in an urban environment, Geophys. J. Int., doi: 10.1111/j.1365-246X.2009.04343.x

Iwan, W. D., M. A. Moser, and C.-Y. Peng, 1985. Some observations on strong-motion earthquake measurement using a digital accelerograph, Bull. Seismol. Soc. Am. 75, 1225–1246.

Louie, J., M. Heimgartner, A. Pancha, W. Thelen, J. Scott, and C. Lopez, 2006, A matter of scale: understanding Nevada's sedimentary basins for seismic hazard assessment: presented at *Seismol. Soc. Amer. Ann. Mtg. and the Managing Risk in Earthquake Country Conference Commemorating the 100th Anniversary of the 1906 Earthquake*, April 18 - 22, San Francisco, Calif.

Lobkis, O. I. and R. L., Weaver. On the emergence of the Green's function in the correlations of a diffusive field, *J. Acoust. Soc. Am.* **110**, 3011-3017 (2001).

Larose, E., A. Derode, D. Clorennec, L. Margerin, and Michel Campillo. Passive retrieval of Rayleigh waves in disordered elastic media, *Phys. Rev.* ***E*** **72**, DOI:10.1103/PhysRevE.72.046607 (2005).

Lin, F. C., Moschetti, M. P. & Ritzwoller, M. H., 2008. Surface wave tomography of the western United States from ambient seismic noise: Rayleigh and Love wave phase velocity maps. *Geophysical Journal International* 173, 281-298.

Louie, J., I. M. Tibuleac and L. Preston, 2010. Basin Model Improvements and Verification for Reno Area, a 3-D Scenario Modeling, final report on grant 08HQGR0046, http://earthquake.usgs.gov/research/external/reports/08HQGR0046.pdf

Pancha, A., J. G. Anderson, and J. N. Louie, 2007. Characterization of Near-Surface Geology at Strong-Motion Stations in the Vicinity of Reno, Nevada, Bulletin of the Seismological Society of America, Vol. 97, No. 6, pp. 2096–2117, December 2007, doi: 10.1785/0120060266.

Preston, L., and D. von Seggern, 2008. Joint Seismic Tomography/Location Inversion in the Reno/Carson City Area, Final Report to the National Earthquake Hazard Reduction Program, U. S. Geological Survey Award Number 07HQGR0022.

Picozzi, M., S. Parolai, D. Bindi and A. Strollo, 2009. Characterization of shallow geology by high-frequency seismic noise tomography, Geophys. J. Int. (2009) 176, 164–174 doi: 10.1111/j.1365-246X.2008.03966.x.

Priestley, K and J. Brune, 1978. Surface waves and the structure of the Great Basin of Nevada and western Utah, JGR, v. 83, pp. 2265-2272.

Ruigrok, E., X. Campmanb, K. Wapenaar, 2011. Extraction of P-wave reflections from microseisms, C. R. Geoscience 343 (2011) 512–525.

Ryberg, T., 2011. Body wave observations from cross ‐ correlations of ambient seismic noise: A case study from the Karoo, RSA, GEOPHYSICAL RESEARCH LETTERS, VOL. 38, L13311, doi:10.1029/2011GL047665, 2011

Sanchez-Sesma, F. J., and M. Campillo, 2006. Retrieval of the Green's function from cross correlation: The canonical elastic problem. *Bull. Seism. Soc. Am*., 96, 1182-1191, doi: 10.1785/0120050181.

Sanchez-Sesma, F. J., A. Rodríguez-Castellanos, Juan J. Pérez-Gavilán, H. Marengo-Mogollón, L. E. Pérez-Rocha and F. Luzón, Some properties of the Green's function of simplified elastodynamic problems, *Earthquakes and Structures* (2012) in press

Sabra, K. G., P. Gerstoft, P. Roux, W. A. Kuperman, and M. C. Fehler, 2005. Surface wave tomography from microseisms in southern California, Geophys. Res. Lett., 32, L14311, doi:10.1029/2005GL023155.Sanchez-Sesma and Campillo, 2006

Scott, J. B., M. Clark, T. Rennie, A. Pancha, H. Park and J. N. Louie, 2004, A shallow shear-wave velocity transect across the Reno, Nevada area basin, Bull. Seism. Soc. Am. 94, no. 6, 2222-2228.

Smith, K., von Seggern, D. H., dePolo, D., Anderson, J. G., Biasi, G. P. , Anooshehpoor, R., (2008), Seismicity of the 2008 Mogul-Somersett West Reno, Nevada Earthquake Sequence, Eos Trans. AGU, 89(53), Fall Meet. Suppl., Abstract S53C-02.

Tibuleac, I. M., D. H. von Seggern, John G. Anderson and J.N. Louie, 2011. Computing Green's Functions from Ambient Noise Recorded by Narrow-Band Seismometers, Accelerometers, and Analog Seismometers, doi: 10.1785/gssrl.82.5.661 *Seismological Research Letters September/October 2011 v. 82 no. 5 p. 661-675.*

Sabra, K. G., P. Gerstoft, P. Roux, W. A. Kuperman, and M. C. Fehler (2005), Surface wave tomography from microseisms in southern California, Geophys. Res. Lett., 32, L14311, doi:10.1029/2005GL023155.

Shapiro, N. M., Campillo, M., Stehly, L., and Ritzwoller, M. H., 2005. High-resolution surface wave tomography from ambient seismic noise, *Science*, 307, 1615-1618.

Tsai, V. C., 2009. On establishing the accuracy of noise tomography travel-time measurements in a realistic medium, *Geophys. J. Int.* 178, 1555–1564

Von Seggern, D.H., Tibuleac, I.M., and Louie, J.N, 2009. Computing Green's Functions from Ambient Noise Recorded by Narrow-Band Seismometers, Accelerometers, and Analog Seismometers, abstract presented at the 2009 Annual Meeting Announcement Seismological Society of America, 8–10 April 2009 Monterey, California

Yang, Y., M.H. Ritzwoller, F.-C. Lin, M.P. Moschetti, and N.M. Shapiro, 2008.The structure of the crust and uppermost mantle beneath the western US revealed by ambient noise and earthquake tomography, J. Geophys. Res., 113, B12310, doi:10.1029/2008JB005833, 2008

Yao, H., R. D. van der Hilst and M. V. de Hoop, 2006. Surface-wave array tomography in SE Tibet from ambient seismic noise and two-station analysis – I. Phase velocity maps, Geophys. J. Int. (2006),166, 732–744

Yao, H., Beghein, C., and Van der Hist, R.D., 2008. Surface-wave array tomography in SE Tibet from ambient seismic noise and two-station analysis: II – Crustal and upper-mantle structure, Geophys. J. Int., Vol. 163, 205-219, doi: 10.1111/j.1365-246X.2007.03696.x.

Weaver, R. L. and O. I., Lobkis, 2004. Diffuse fields in open systems and the emergence of the Green's function. *J. Acoust. Soc. Am.*, 116, 2731-2734

Wapenaar, K., 2004. Retrieving the elastodynamic Green's function of an arbitrary inhomogeneous medium by cross-correlation: Physical Review Letters, 93, 254301.

ACKNOWLEDGEMENTS

We thank Dr Hafidh Ghalib for generously sharing his surface wave expertise and his group velocity tomography algorithms. We thank Drs. John Louie and Ken Smith, their students (including Annie Kell-Hills, Mahesh Dhar and Mayo Thompson) and the Reno residents for organizing, and making possible the 2008 short period deployment in the Reno Basin. We are indebted to Mahesh Dhar and to Dr Ken Smith, who built the database for the high frequency geophone survey in 2008. We thank Drs. Glenn Biasi and Rasool Anoshepoor for help with database building and broadband instrument installation in Mogul. We are grateful to the Nevada Seismological Laboratory faculty and technical personnel who contributed to the acquisition of the extensive temporary and permanent station database used in this study. We thank Dr. John G. Anderson for advice and encouragement.

PUBLICATIONS

Two publications resulted from this award:

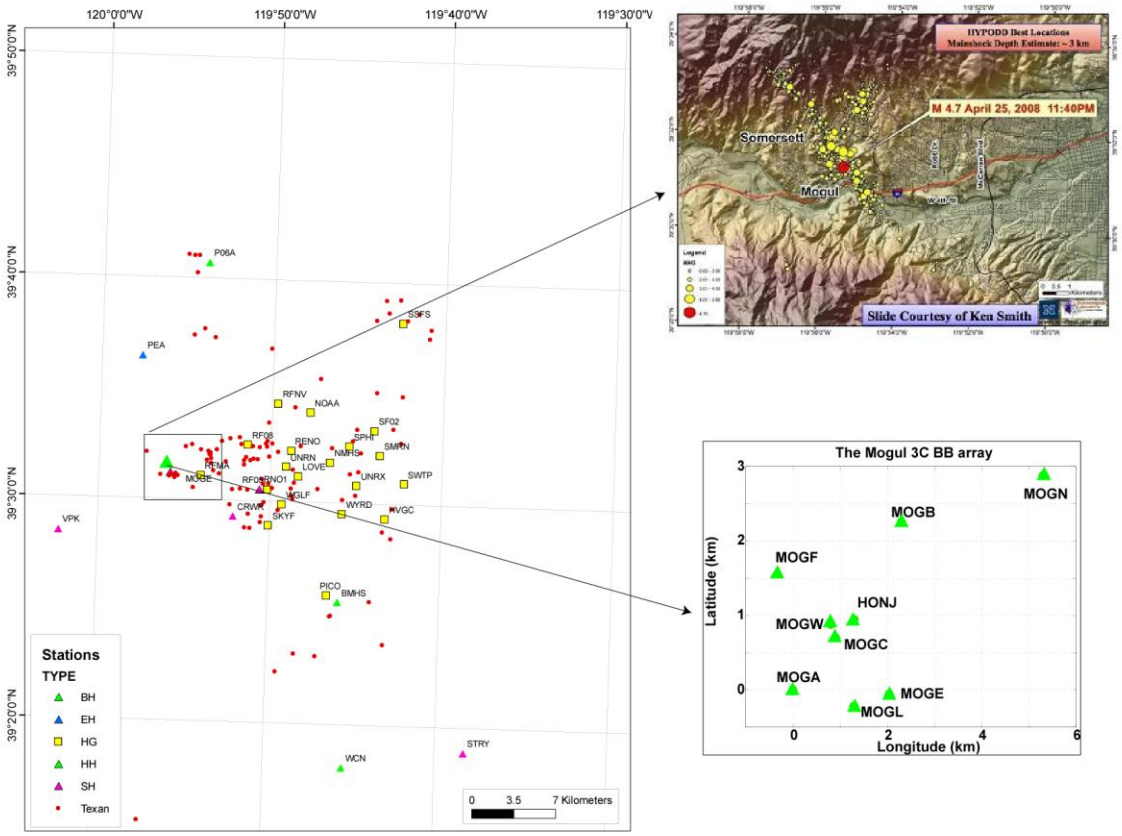

Figure 1 shows permanent stations (see legend for station type), temporary stations with high-frequency geophones and "Texan" digitizers (red dots) and a map of the Rapid Array Mobilization Program deployment (green triangle in the left plot and right bottom plot) in the Reno-Carson, NV area. Seismic events in the Reno Basin occurred in 2008 are shown in the upper right plot. The upper right plot shows HYPODD relocated earthquakes that occurred in 2008 in the Mogul – Somersett residential area, west of Reno (Smith et al., 2008). The spatial distribution of the subset relocated here is representative of the locations of nearly all earthquakes in the sequence.

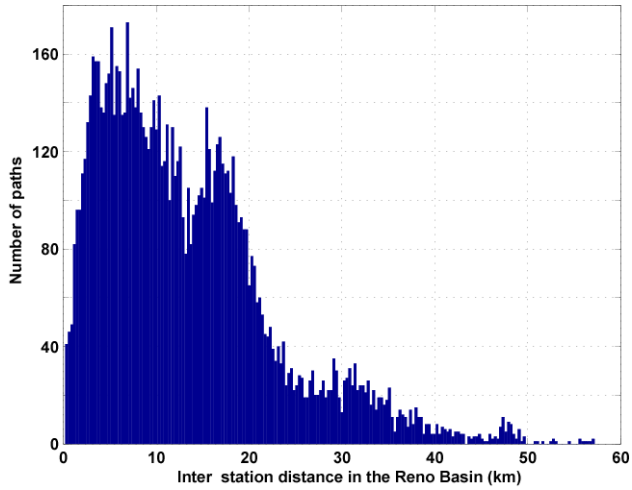

Figure 2. Inter-station distance in the Reno Basin.

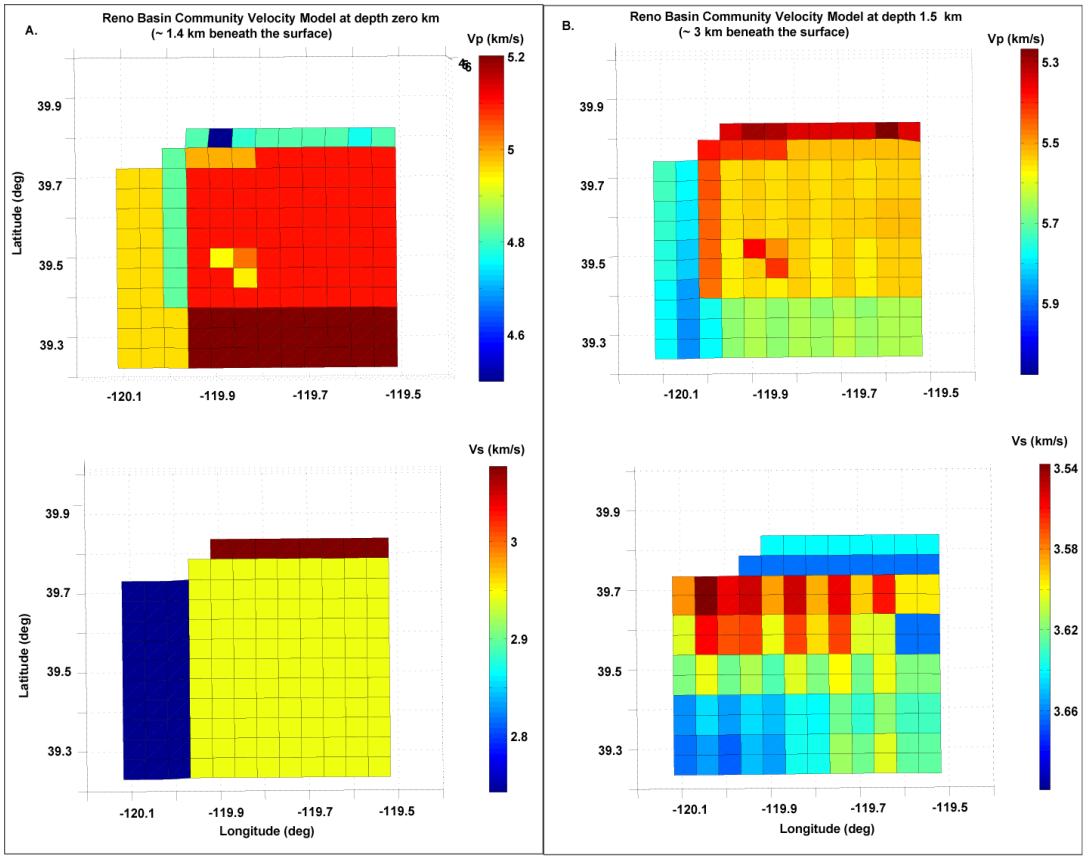

Figure 3. Shows the preliminary velocity model at zero km depth (inset A) and at 1.5 km depth (inset B) in the Reno Basin. Depth is zero at the sea level and positive below the sea level. In each inset the upper plot shows P -velocity and the lower plot shows S-velocity. Note that these models include the CVM and results from Tibuleac et al, 2011 (Part 1 of this report), as well as shear wave velocity from a previous ambient noise analysis study in Louie, Tibuleac and Preston, 2010.

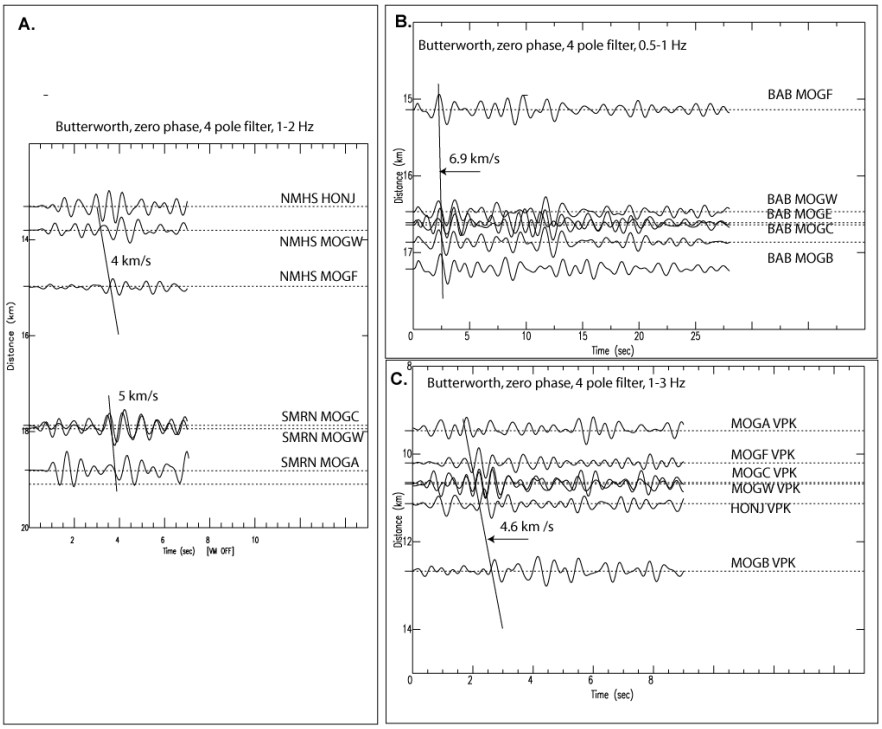

Figure 4. Waveforms interpreted as the P-component of the inter-station Green's Functions for paths between the Mogul array and accelerometers (left plot) and the Mogul array and short-period sensors (right plots). Note different frequency bands, as a function of the sensor type, path and distance and low SNR P-arrivals, which makes identification difficult, unless the waveforms were recorded at array of sensors (in this case the Mogul array).

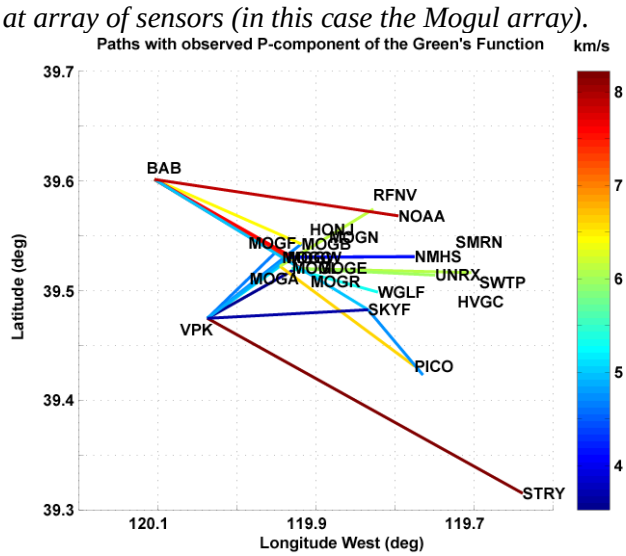

Figure 5. Shows P- phase velocity for inter-station paths in the study area.

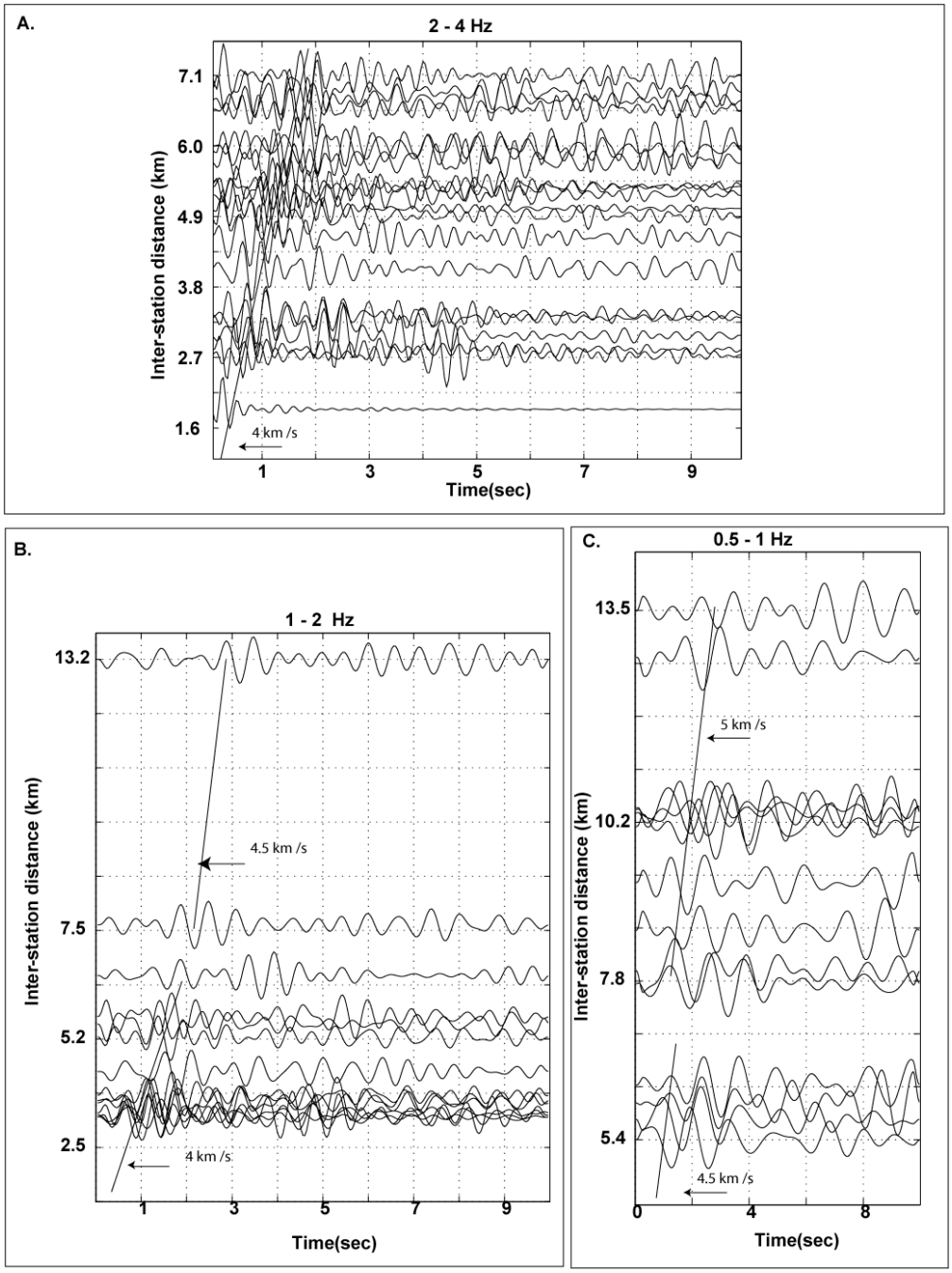

Figure 6. Waveforms interpreted as the P-component of the inter-station Green's Functions for paths between stations including geophones (see also Table 2). The SNR of all arrivals is larger than 1.1. Note most P-energy in the 2-4 Hz frequency band up to 7 km distance and low energy arrivals in the bands 1-2 Hz and 0.5 - 1 Hz up to 15 km inter-station distance. All waveforms were filtered with a Butterworth, zero phase, eight pole filter except for the 0.5 - 1 Hz frequency band, where a six pole filter was used.

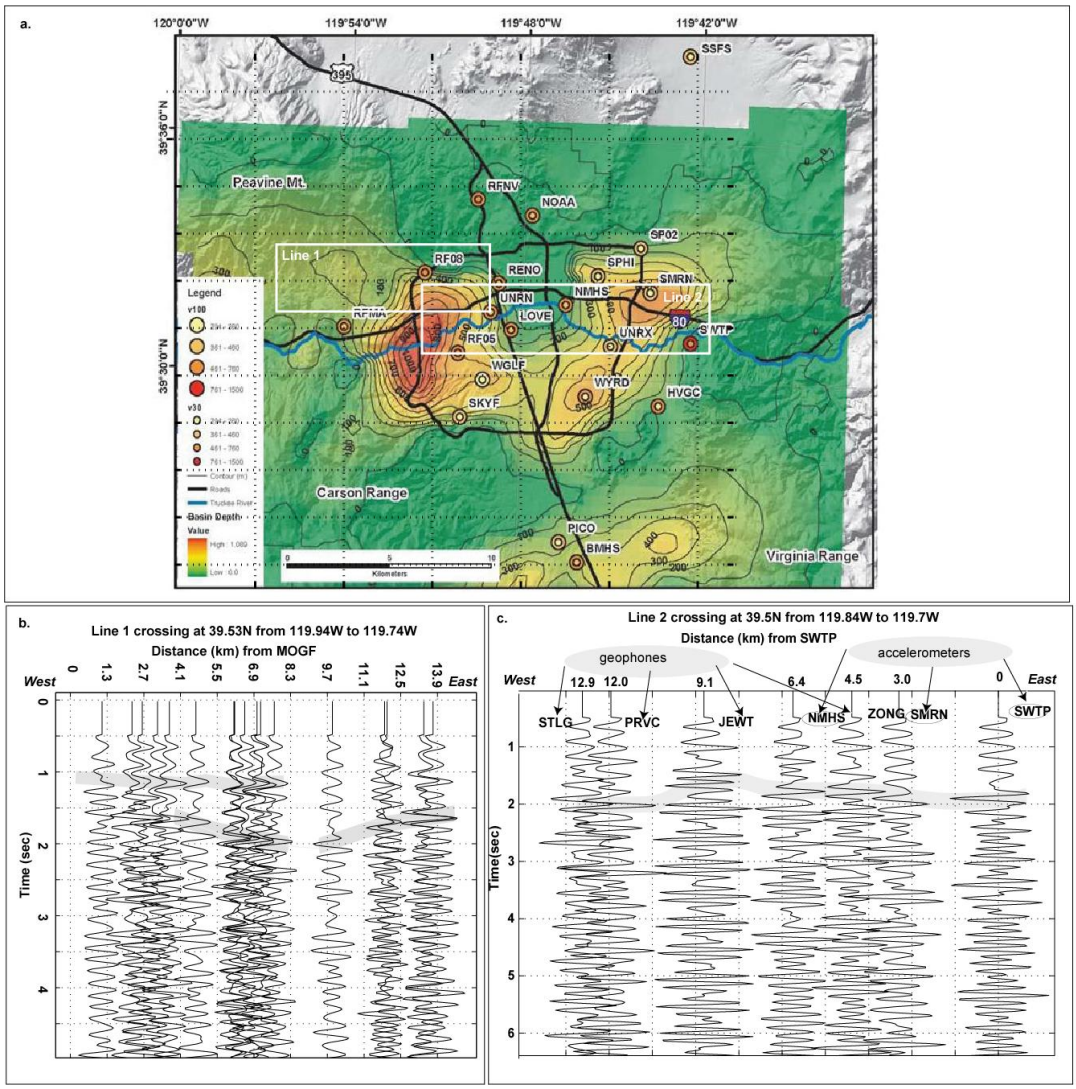

Figure 7. a). The background (from Pancha et al., 2007) shows a basin-depth model from Abbott and Louie (2000), based on gravity observations. Contours are 100 m. Our results are consistent with these estimates. The white rectangles show the location of the approximately linear groups of stations named Lines 1 and 2. b) Reno Basin autocorrelations estimated using three days to three months of records in 2008. Waveforms are filtered from 4 to 8 Hz with an 8-pole, zero phase Butterworth filter and the AGC window is 1 sec. Beneath the Mogul array a clear arrival at 1 sec is observed. This arrival is replaced by a 1-5 - 2 s arrival within the basin at distances from MOGF greater than 8.5 km. c). Same as in Figure 7b, for Line 2. The larger amplitude arrivals at ~ 2 sec are interpreted as reflections from a layer ~ 1.5 km deep, at the bottom of the Reno Basin. Note that the waveforms were not corrected for elevation. Maxim elevation corrections for 150 m elevation difference are ~ 0.2 s.

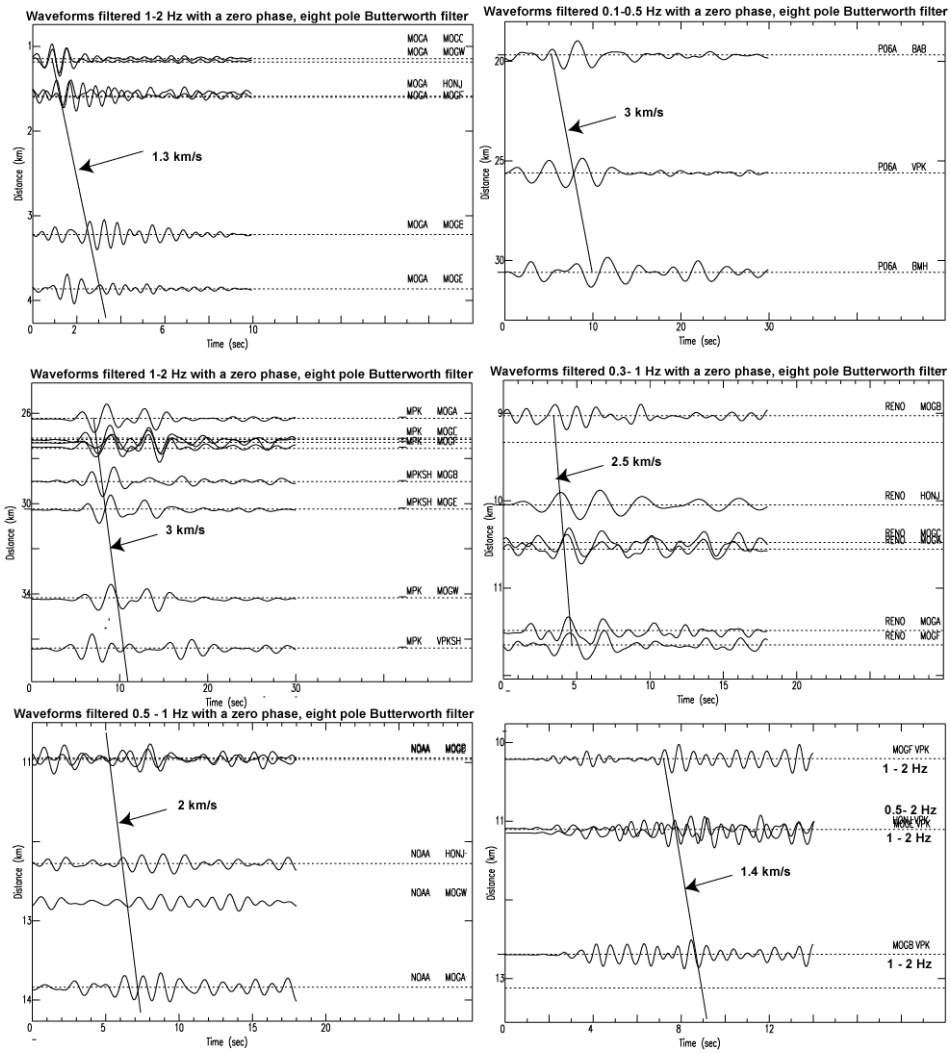

Figure 8. Example of GF fundamental Rayleigh extracted in the Reno Basin for station pairs including all the sensors except for geophones. Note different filters, as a function of inter-station distance and different abscise scale.

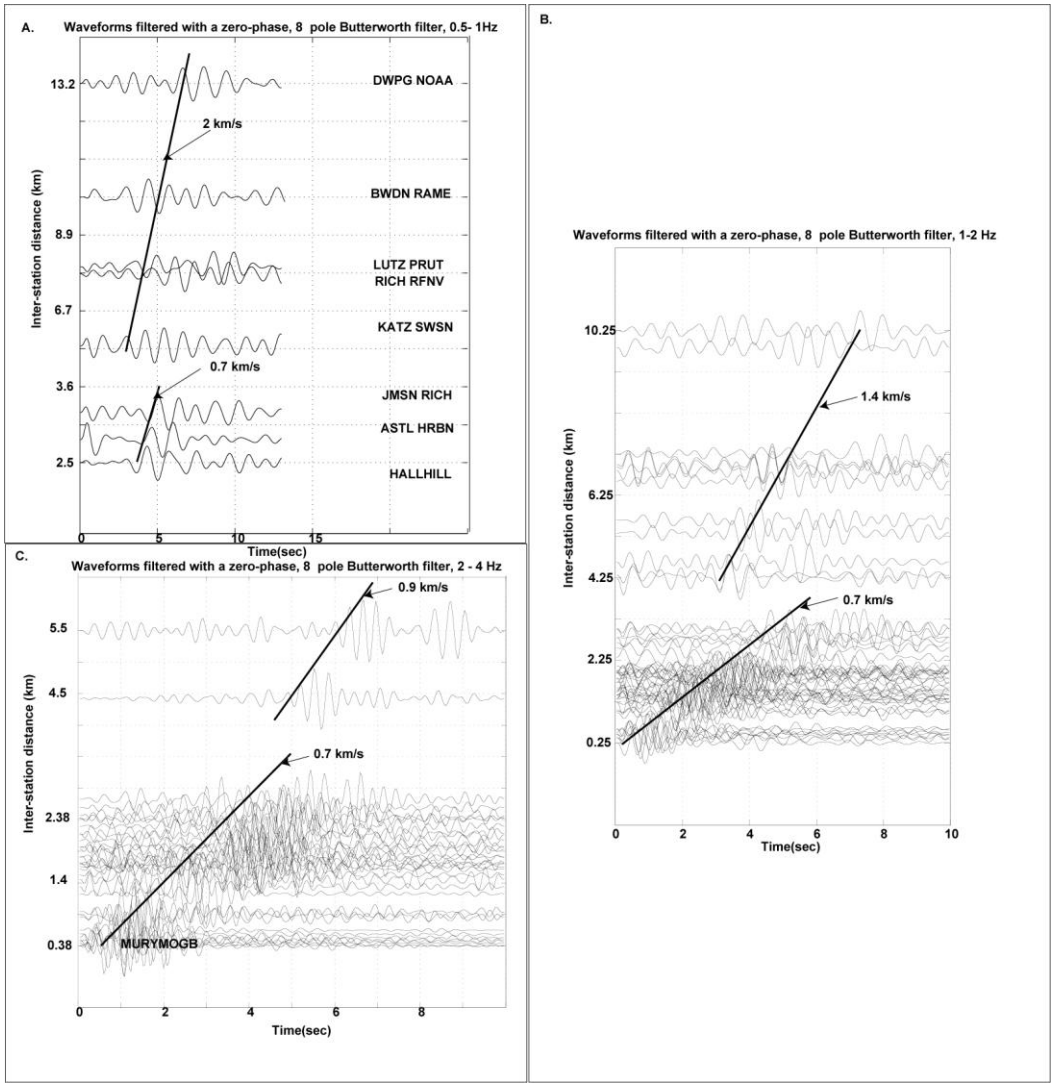

Figure 9. Example of GF fundamental Rayleigh extracted in the Reno Basin for station pairs including geophones for three frequency bands. Note lower SNR for the longer periods.

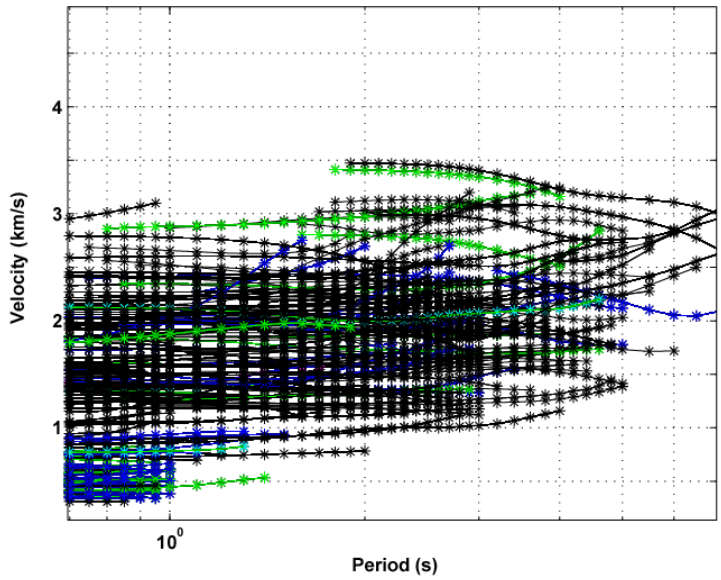

Figure 10. Dispersion curves extracted in the Reno Basin on 230 paths. Green is for dispersion curves extracted between station pairs to the southeast, blue is for station pairs in the northwest, cyan is for station pairs to the southeast and black is for station paths crossing the Reno Basin.

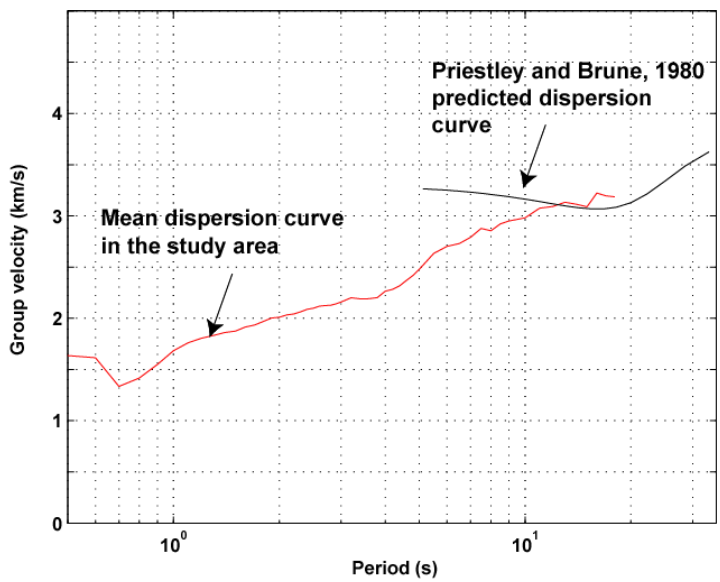

Figure 11. Comparison of the mean model derived from fundamental Rayleigh group velocity curves in the study area and the dispersion curves estimated from a Nevada model in Priestley and Brune, 1980.

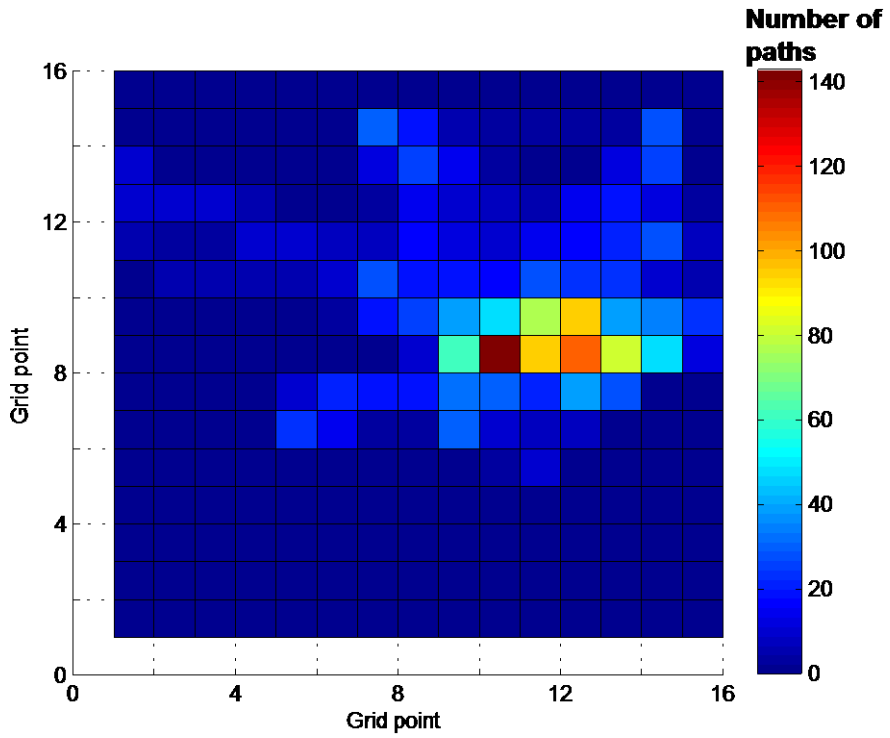

Figure 12. Number of paths used for tomographic inversion per grid element. The first grid element (1,1) starts at 39.2N, 120.3W and the interval between points is 0.04 deg.

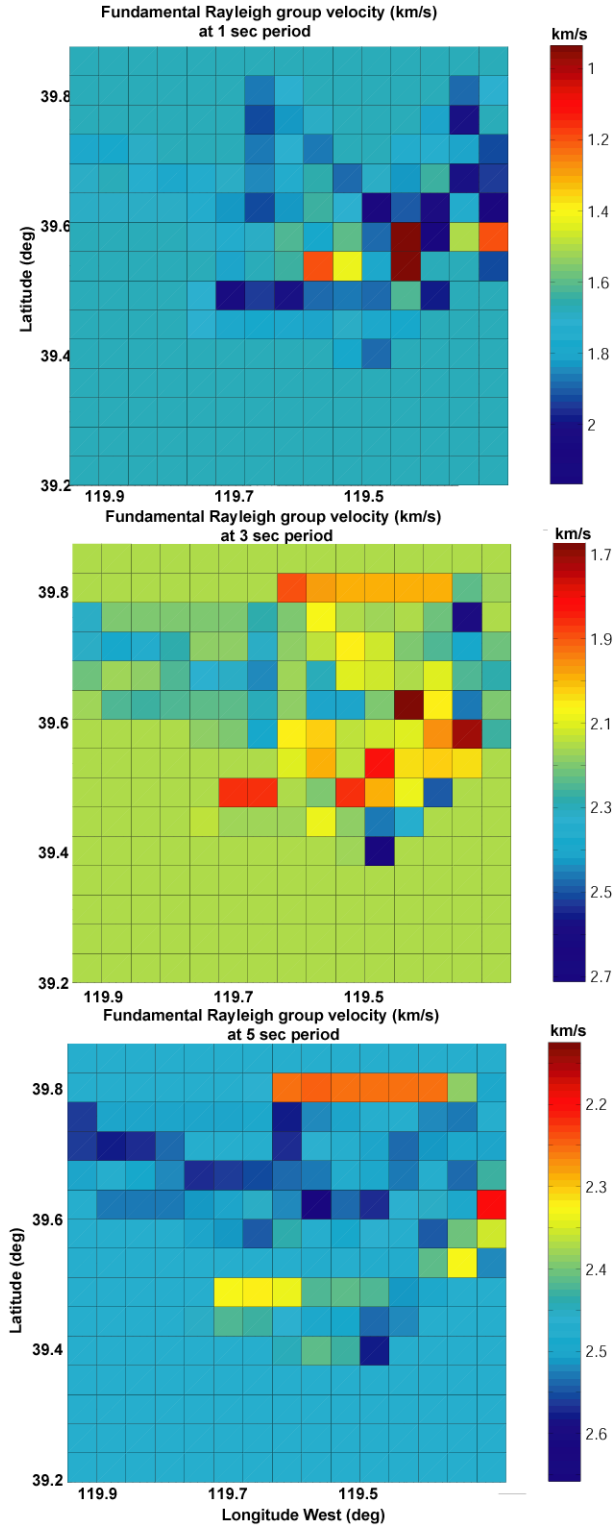

Figure 13. Fundamental Rayleigh group velocity maps of the study area at the periods of 1 s, 3 s and 5 s. Note high group velocity variability at 1s period (left upper plot) compared to longer periods. Large velocity contrast was observed at the eastern boundary of the Reno Basin. Different color scales are used for group velocity values in each plot. At all periods, higher group velocity corresponds to the Sierra Nevada mountain range. Lower velocity features correspond to well-known geothermal fields around Reno and, at 3s period, to the Reno Basin.

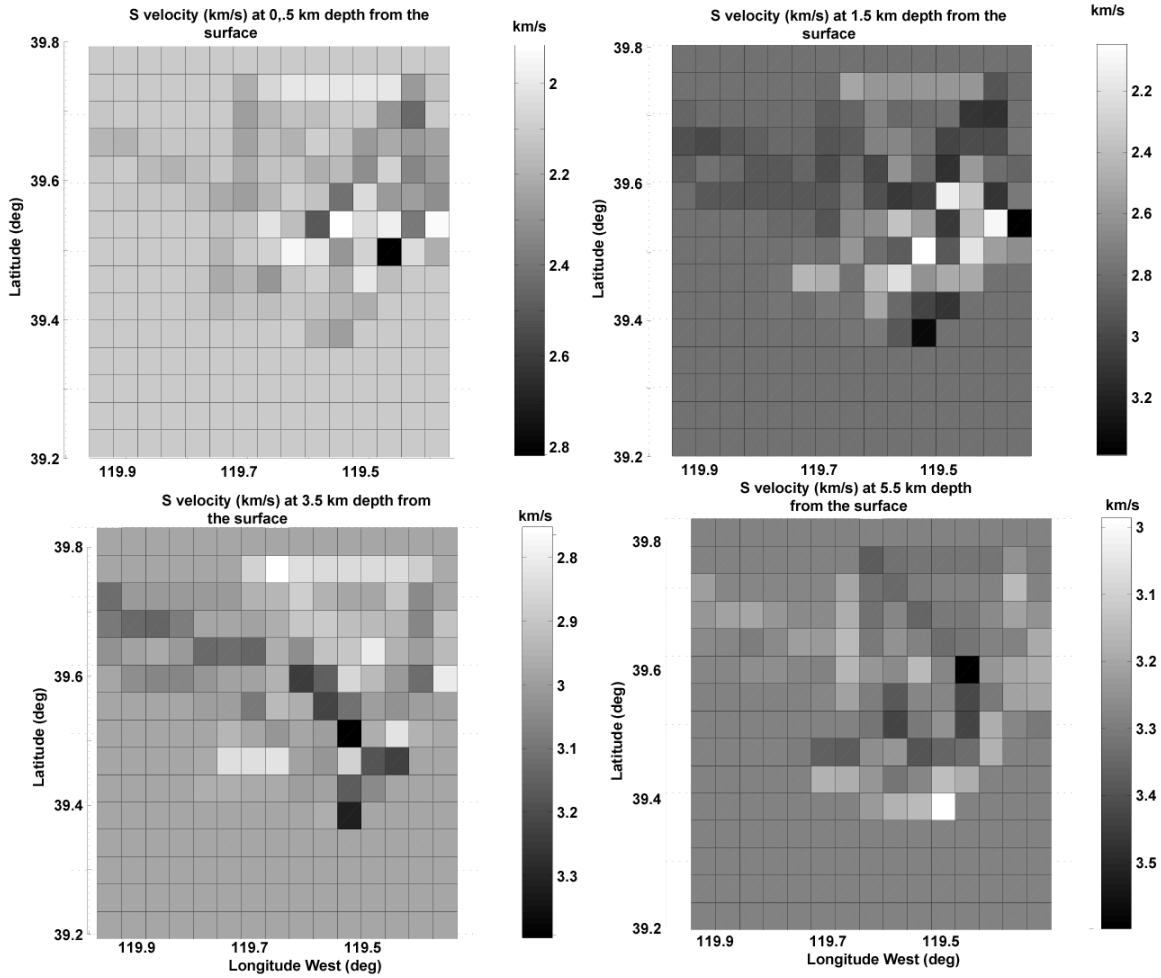

Figure 14. Shear wave velocity models extracted at each grid point from the group velocity maps in Figure 13. The mean station elevation was -1.4 km. A gray scale was found appropriate to show shear velocity values, since the Reno Basin is a feature better observed at 1.5 and 3.5 km depth from the surface (right upper plot and left lower plot). Higher S- velocity corresponds to the Sierra Nevada mountain range to depths of 5 km. Lower S-velocity features correspond to well-known geothermal fields in the study area.

Table 1. Location of the stations used in this study. "SH" are analog short-period sensors, "BH" and "HH" are broadband sensors and "E" are short period sensors.

CRWR	SH	39.4883	-119.8683	1.484
BMHS	HH	39.4231	-119.7648	1.394
HONJ	HH	39.5307	-119.9302	1.6000
WCN	BH	39.3017	-119.7563	0
BAB	SH	39.6013	-120.1040	0
MPK	SH	39.2957	-120.0302	0
PEA	EH	39.6076	-119.9603	0
VPK	SH	39.4747	-120.0373	0
P06A	BH	39.6785	-119.8983	1.3686
MOGL	HH	39.5202	-119.9304	1.4680
MOGL	SH	39.5202	-119.9304	1.4680
MOGE	HH	39.5217	-119.9216	1.4500
MOGW	HH	39.5301	-119.9360	1.5840
MOGA	HH	39.5222	-119.9454	1.4660
MOGR	HH	39.5084	-119.9070	1.4060
MOGF	HH	39.5362	-119.9492	1.5890
MOGN	HH	39.5481	-119.8836	1.6040
MOGC	HH	39.5285	-119.9348	1.569
MOGB	HH	39.5425	-119.9186	1.605
GSCB	HG	39.2267	-120.0812	1.8998
HVGC	HG	39.4897	-119.7209	1.3720
NMHS	HG	39.5309	-119.7754	1.3800
NOAA	HG	39.5681	-119.7958	1.4900
PICO	HG	39.4312	-119.7756	1.3810
RENO	HG	39.5391	-119.8138	1.3840
RF05	HG	39.5095	-119.8360	1.4000
RF08	HG	39.5427	-119.8561	1.4720
RFMA	HG	39.5188	-119.9010	1.5180
RFNV	HG	39.5742	-119.8275	1.5440
RNO1	SH	39.5093	-119.8434	1.3910
SF02	HG	39.5557	-119.7334	1.3800
SMRN	HG	39.5372	-119.7274	1.3690
SPHI	HG	39.5436	-119.7573	1.3590
SSFS	HG	39.6370	-119.7083	1.3200
STRY	SH	39.3151	-119.6386	1.8397
SWTP	HG	39.5164	-119.7035	1.3850
UNRN	HG	39.527	-119.818	1.3900
UNRX	HG	39.5141	-119.7493	1.3180
WGLF	HG	39.4986	-119.8216	1.4130
WYRD	HG	39.4927	-119.7628	1.3730
SKYF	HG	39.4825	-119.8340	1.5520
RAME	EH	39.5048	-119.8120	1.3780
MCMI	EH	39.4799	-119.8520	1.5710
RICH	EH	39.5084	-119.8700	1.4050
YAWN	EH	39.5200	-119.8830	1.4810
SHOP	EH	39.5414	-119.8370	1.4370
WLS1	EH	39.5105	-119.7870	1.3500
PTSN	EH	39.5375	-119.8260	1.4080
ASTL	EH	39.4970	-119.8720	1.4810
SDMN	EH	39.5101	-119.8130	1.3710
MRSL	EH	39.4969	-119.8420	1.4520
JMSN	EH	39.5376	-119.9010	1.6220
COS1	EH	39.5137	-119.8350	1.3840
WHIT	EH	39.5314	-119.8910	1.5150
MACG	EH	39.5341	-119.8920	1.5220
HRBN	EH	39.5166	-119.8410	1.3850
GLAS	EH	39.5445	-119.8810	1.5760
TBDZ	EH	39.5407	-119.8440	1.4480
HALL	EH	39.2582	-119.9531	2.1410
LOUE	EH	39.5439	-119.8320	1.4310
CSON	EH	39.3724	-119.8230	1.7020
BWDN	EH	39.5414	-119.9100	1.6100
TYLR	EH	39.3864	-119.8060	1.6610
SWSN	EH	39.5594	-119.8359	1.5110

GILT	EH	39.5345	-119.8930	1.5230
GRSD	EH	39.6151	-119.8350	1.5470
ETLS	EH	39.5561	-119.7500	1.3510
WABL	EH	39.5414	-119.7740	1.3540
STLG	EH	39.5303	-119.8590	1.4630
BART	EH	39.5301	-119.8950	1.5430
JKSN	EH	39.5026	-119.8110	1.3790
BLAK	EH	39.4904	-119.8540	1.5510
DHAR	EH	39.5425	-119.8044	1.3720
BLEY	EH	39.6286	-119.9008	1.5540
PRVC	EH	39.5316	-119.8460	1.4470
CASH	EH	39.5083	-119.8550	1.3990
MURY	EH	39.5396	-119.9160	1.5870
ZLFQ	EH	39.3850	-119.7850	1.5450
EWD1	EH	39.5713	-119.8110	1.4910
TREX	EH	39.5130	-119.8400	1.3880
RAEL	EH	39.5354	-119.8920	1.5310
HILL	EH	39.2426	-119.9320	1.9650
TNG1	EH	39.6836	-119.9080	1.5470
TNG2	EH	39.6837	-119.9126	1.5810
TNG3	EH	39.6842	-119.9186	1.5810
RGSK	EH	39.5381	-119.7460	1.3430
GONZ	EH	39.5457	-119.8370	1.4510
SHRP	EH	39.5460	-119.7070	1.3430
MCLG	EH	39.4940	-119.8250	1.4110
SMIT	EH	39.6221	-119.8904	1.5800
WATT	EH	39.5304	-119.8530	1.4640
DAVI	EH	39.5466	-119.8730	1.5590
WLN2	EH	39.5271	-119.8590	1.4670
CGNY	EH	39.5092	-119.8620	1.3990
DKRY	EH	39.5931	-119.7870	1.4540
BRWN	EH	39.2561	-119.9718	2.0450
STFL	EH	39.6236	-119.9110	1.5720
COG1	EH	39.5028	-119.7630	1.3420
COG2	EH	39.4152	-119.7720	1.4620
COG3	EH	39.4268	-119.7340	1.3630
KIRK	EH	39.5435	-119.8380	1.4510
ZABA	EH	39.5472	-119.7540	1.3470
DMRS	EH	39.3948	-119.7200	1.4240
PROT	EH	39.4794	-119.7230	1.3520
WILM	EH	39.4154	-119.7710	1.4220
ZONG	EH	39.5221	-119.7560	1.3440
CNRS	EH	39.5093	-119.9080	1.4230
LUTZ	EH	39.5338	-119.8350	1.4090
JEWT	EH	39.5145	-119.8100	1.3650
KNUS	EH	39.5317	-119.8500	1.4560
FENE	EH	39.5161	-119.9260	1.4380
BLEG	EH	39.5064	-119.7500	1.3390
PEST	EH	39.5350	-119.9540	1.6100
BARN	EH	39.4969	-119.7140	1.3720
NAGY	EH	39.5291	-119.8770	1.4980
JRDN	EH	39.5475	-119.8640	1.5430
DWPG	EH	39.5183	-119.9400	1.4890
DCZR	EH	39.6708	-119.9096	1.5350
HMND	EH	39.4886	-119.8410	1.4930
DOUG	EH	39.4745	-119.7150	1.4020
KRIN	EH	39.5380	-119.8860	1.5520
ROSS	EH	39.4800	-119.8570	1.6060
HWKN	EH	39.5330	-119.8570	1.4740
PRIC	EH	39.4994	-119.8390	1.4410
KATZ	EH	39.5223	-119.8888	1.4900
DONH	EH	39.5367	-119.8940	1.5410
MEYR	EH	39.5103	-119.8310	1.3970
SHER	EH	39.5566	-119.7150	1.3460
COOT	EH	39.5178	-119.9230	1.4320
WILD	EH	39.4844	-119.8420	1.5050

PRUT	EH	39.5187	-119.9300	1.4430
MANC	EH	39.5171	-119.9310	1.4420
SINA	EH	39.5412	-119.8510	1.4720
PALM	EH	39.5278	-119.8910	1.5210
LICO	EH	39.5193	-119.9250	1.4370
BEAS	EH	39.5813	-119.7070	1.4210
WKSN	EH	39.6383	-119.7340	1.3960
SPLD	EH	39.5840	-119.7320	1.3950
SAVA	EH	39.6543	-119.7110	1.3780
VAGO	EH	39.6253	-119.6820	1.3720
NASH	EH	39.6322	-119.6810	1.3770
SWAN	EH	39.6536	-119.7250	1.3780
FBRG	EH	39.6439	-119.7220	1.3740
SPAN	EH	39.6441	-119.6930	1.3790
MCCL	EH	39.6385	-119.7040	1.3710

Table 2. Sensor pairs used in Figures 6 and 9.

Pairs of stations	Inter-station distance (km)
Figure 6, A	
BWDN GILT	1.6468
CNRS FENE	1.7187
CGNY TREX	1.9330
TREX WATT	2.2315
RICH WLN2	2.2819
DAVI KIRK	3.0191
LOUE DAVI	3.5260
PRIC STLG	3.8379
FENE MOGE	3.9737
ASTL BART	4.1730
KIRK SDMN	4.2851
KATZ MOGE	4.3097
LOUE RAME	4.6710
PRIC KIRK	4.9009
GILT GONZ	4.9576
SHRP BARN	5.4892
KIRK MCLG	5.6121
CNR SPRIC	6.0173
Figure 6,B	
TBDZ TREX	3.0969
LOUE TREX	3.5012
BLEG RGSK	3.5391
RAEL RICH	3.5435
LUTZ CGNY	3.5815
MEYR SINA	3.8375
MRSL PRVC	3.8713
CASH SHOP	3.9887
GONZ SDMN	4.4584
LUTZ ASTL	5.1750
JKSN SINA	5.4910
BLAK SINA	5.6508
SDMN ZABA	6.5245
JRDN ROSS	7.5247
COG3 WABL	13.1885
Figure 6, C	
KATZ MOGF	5.4024
ASTL UNRN	5.7047
SWSN YAWN	5.9548
COS1 JMSN	6.2496
WATT MOGA	7.9718
HMND PICO	8.4956
ASTL RFNV	9.3878
LUTZ PEST	10.1995
DAVI ZONG	10.3904
GRSD WHIT	10.4649
JRDN SHER	12.8063

DWPG NOAA	13.5393
Figure 9, C	
GILT WHIT	0.3849
MURY MOGB	0.3918
TREX HRBN	0.4094
RAEL WHIT	0.4528
ZABA SPHI	0.4902
BART GILT	0.5179
SDMN JEWT	0.5525
WLN2 WATT	0.6319
MEYR TREX	0.8275
DWPG PRUT	0.8585
PROT DOUG	0.8763
PRVC WLN2	1.2213
JKSN JEWT	1.3249
DAVI KRIN	1.4679
PRIC TREX	1.5136
ASTL CGNY	1.6041
MCLG RAME	1.6379
CASH PRIC	1.6916
SINA WLN2	1.7103
STLG TBDZ	1.7285
BLEG ZONG	1.8185
LOUE PRVC	1.8185
ASTL CASH	1.9237
MRSL COS1	1.9610
TBDZ WLN2	1.9839
MCLG SDMN	2.0637
GONZ WATT	2.1841
MRSL HRBN	2.1911
KIRK STLG	2.3218
TREX UNRN	2.4444
WLN2 SHOP	2.4660
MCLG TREX	2.4722
LICO MOGB	2.6358
LOUE STLG	2.7636
JRDN RICH	4.3752
BLEG ETLS	5.5224
Figure 9, B	0.3849
GONZ KIRK	0.2591
STLG WLN2	0.3556
MURY MOGB	0.3918
RAEL WHIT	0.4528
GONZ LOUE	0.4726
KIRK LOUE	0.5158
SDMN JEWT	0.5525
KIRK TBDZ	0.6013
LUTZ PRVC	0.9740
MCMI WILD	0.9924
PRVC TBDZ	1.0254
BLAK MCMI	1.1791
PRVC WLN2	1.2213
ASTL RICH	1.2781
LUTZ GONZ	1.3336
PRVC SHOP	1.3346
CASH TREX	1.3885
PRIC MEYR	1.3916
MURY MOGE	1.4276
KIRK PRVC	1.4894
CASH HRBN	1.5137
BWDN MOGE	1.5157
LUTZ SINA	1.5988
CASH PRIC	1.6916
SINA WLN2	1.7103
MEYR MRSL	1.7627
LOUE PRVC	1.8185

ASTL CASH	1.9237
CGNY TREX	1.9330
KIRK WATT	1.9419
MRSL COS1	1.9610
DAVI SINA	1.9787
CGNY HRBN	1.9789
TBDZ WLN2	1.9839
GONZ RENO	2.1190
KIRK STLG	2.3218
PRICS DMN	2.5259
HRBN RICH	2.6478
BLAK TREX	2.7837
GONZ WLN2	2.7978
MEYR BLAK	2.9627
PRICJ EWT	2.9994
CGNY SDMN	4.2017
CGNY KIRK	4.3310
BLAK PRVC	4.6295
LOUE MRSL	5.2926
BLAK TBDZ	5.6547
SINA WABL	6.5980
MRSL NMHS	6.8466
MRSL SWSN	6.9647
SWSN MRSL	6.9647
GONZ MOGE	7.2796
SPLD BARN	9.8009
PRIC PROT	10.1927
Figure 9, A	0.2591
HALL HILL	2.5106
ASTL HRBN	3.4360
JMSN RICH	4.1939
KATZ SWSN	6.1274
RICH RFNV	8.1686
LUTZ PRUT	8.3137
BWDN RAME	9.3334
DWPG NOAA	13.5393

Table 3 Location of the stations used in Figure 7.

Line 1		
39.5362	-119.9492	MOGF
39.5222	-119.9454	MOGA
39.5301	-119.9360	MOGW
39.5285	-119.9348	MOGC
39.5517	-119.9216	MOGE
39.5425	-119.9186	MOGB
39.5396	-119.9160	MURY
39.5414	-119.9100	BWDN
39.5354	-119.8920	RAEL
39.5376	-119.9010	JMSN
39.5445	-119.8810	GLAS
39.5301	-119.8950	BART
39.5345	-119.8930	GILT
39.5341	-119.8920	MACG
39.5314	-119.8910	WHIT
39.5200	-119.8830	YAWN
39.5271	-119.8590	WLN2
39.5303	-119.8590	STLG
39.5304	-119.8530	WATT
39.5316	-119.8460	PRVC
39.5338	-119.8350	LUTZ
39.527	-119.818	UNRN
39.5407	-119.8440	TBDZ
39.5466	-119.8730	DAVI
39.5435	-119.8380	KIRK
39.5414	-119.8370	SHOP
39.5457	-119.8370	GONZ

39.5439	-119.8320	LOUE
39.5391	-119.8138	RENO
39.5425	-119.8044	DHAR
39.5414	-119.7740	WABL
39.5436	-119.7573	SPHI
39.5472	-119.7540	ZABA
39.5221	-119.7560	ZONG
39.5309	-119.7754	NMHS
39.5561	-119.7500	ETLS
39.5381	-119.7460	RGSK
39.5164	-119.7035	SWTP
39.5372	-119.7274	SMRN
39.5309	-119.7870	ZONG
39.5145	-119.8130	NMHS
39.527	-119.8310	JEWT
39.5317	-119.8500	PRVC
39.5330	-119.8570	STLG

Table 4 The mean fundamental Rayleigh group velocity dispersion curve for the study area

Period (s)	S velocity (km/s)
0.5	1.63
0.6	1.61
0.7	1.33
0.8	1.41
0.9	1.55
1.0	1.68
1.1	1.76
1.2	1.80
1.3	1.83
1.4	1.86
1.5	1.87
1.6	1.91
1.7	1.93
1.8	1.96
1.9	2.00
2.0	2.01
2.09	2.03
2.2	2.04
2.3	2.06
2.40	2.08
2.5	2.09
2.59	2.11
2.7	2.12
2.8	2.12
2.90	2.14
3.0	2.15
3.2	2.20
3.40	2.18
3.59	2.19
3.8	2.20
4.0	2.26
4.18	2.28
4.40	2.31
4.59	2.37
4.80	2.41
5.0	2.47
5.5	2.63
6.0	2.70
6.5	2.72
7.0	2.79
7.5	2.87
8.0	2.85
8.5	2.92
9.0	2.94
9.5	2.96
10.	2.98

11.	3.07
12.	3.09
13.	3.13
14.	3.11
15.	3.08
16.	3.22

Table 5. The starting model for the surf96 velocity inversion in the study area

Layer thickness (km)	*Vp (km/s)*	*Vs(km/s)*	*Rho (kg/m^3)*	*Qp*	*Qs*
1	*3.8*	*2.2*	*1.8*	*100*	*50*
1	*3.8*	*2.2*	*1.9*	*100*	*50*
2	*4*	*2.45*	*2.2*	*100*	*50*
2	*5.4*	*2.87*	*2.59*	*450*	*225*
2	*6.4*	*3.67*	*2.82*	*450*	*225*
16.5	*7.4*	*3.87*	*2.82*	*450*	*225*
0	*7.5*	*3.95*	*2.84*	*900*	*540*